

**Visibility Model Verification
by Image Processing Techniques**

by

**Susan M. Larson and Glen R. Cass
Environmental Quality Laboratory
California Institute of Technology**

and

**Kevin J. Hussey and Frederick Luce
Jet Propulsion Laboratory
California Institute of Technology**

October 31, 1984

**Environmental Quality Laboratory
California Institute of Technology
Pasadena, California 91125**

Final Report to the

STATE OF CALIFORNIA
AIR RESOURCES BOARD

in

completion of research under
ARB Contract No.
A2-077-32

Disclaimer

The statements and conclusions in this report are those of the authors and not necessarily those of the California Air Resources Board. The mention of commercial products, their source or their use in connection with material reported herein is not to be construed as either an actual or an implied endorsement of such products.

Executive Summary

Visibility reduction due to air pollutants is particularly severe in urban areas like Los Angeles with many pollution sources and unfavorable meteorology. Air pollution abatement programs can be designed to improve visibility, but to do so in a deliberate fashion requires accurate, verified models which predict the effects on visibility of altering the air pollutant mixture. This study investigates visibility modeling methods that use simulated photographs to display the results of the visibility calculations. Visibility models of this kind are in their infancy at present and have never before been tested to confirm their accuracy in representing the appearance of heavy urban photochemical smog conditions. The purpose of this project is to apply image processing-based visibility modeling methods to Los Angeles regional haze conditions and to develop methods for testing the accuracy of this type of visibility modeling approach.

Visibility reduction is caused by scattering and absorption of light by particulate matter and by gases in the atmosphere. The Lambert law of attenuation describes this decrease in light from object to observer:

$$I(s) = I(o) e^{-b_{\text{ext}} s} \quad (i)$$

where $I(s)$ is the observed intensity at a distance, s , from the object; $I(o)$ is the unattenuated intensity at the object; s is the

path length; b_{ext} is the extinction coefficient and accounts for light extinction due to absorption by particles, scattering by particles, absorption by gases, and scattering by gases. Light reaching an observer along a particular line of sight either could have come from the target viewed or could have been scattered into the line of sight. A second equation can be developed which includes not only light from the target but also skylight which is scattered into the line of sight:

$$I(s) = I(o) e^{-b_{\text{ext}}s} + I_{\text{sky}}(1 - e^{-b_{\text{ext}}s}) \quad (\text{ii})$$

where I_{sky} is the intensity of the horizon sky.

Equation (ii) can be used as the basis for a visibility model that produces synthetic photographs of the appearance of a scene under prescribed air pollutant loading conditions (Malm, 1983). Such a model begins with a photograph taken under very clear conditions. This is the base photograph. This base photograph is broken down into a matrix of millions of small picture elements. The color and brightness values of these picture elements are stored in a computer. Smog is "added" to this base photograph by modifying the color and brightness of each picture element in accordance with equation (ii). The modified image can be played back onto color negative film to produce a synthetic photograph of the smog condition being simulated.

The accuracy of the results obtained by previous investigators using this type of visibility modeling approach has not been tested extensively. In the present study, model verification tests will be

devised based on comparing synthetic photographs to actual photographs taken under the conditions modeled.

In order to verify a mathematical modeling approach, it is necessary to obtain a high quality set of the input data on pollutant loading and visual appearance required by the model. An experimental program was developed in order to characterize the physical and chemical characteristics of the particulate matter and gaseous pollutants present in the atmosphere on a very clean day and on a very smoggy day in Pasadena, California.

During the experiments, standard photographs were taken of chosen scenes. The clean day image provides the substrate on which the synthetic smog calculations are performed, while the heavy smog day photographs will be compared to synthetic images produced by the visibility model. The physical and chemical information on pollutant properties obtained both on the clean and on the smoggy day was used to calculate the volume average refractive index of the aerosol and then the extinction coefficient for each event. The extinction coefficient, b_{ext} , is needed in equation (ii). Both $I(o)$ and I_{sky} are determined from the clear-day photograph. The distance to objects, s , was determined using topographic maps and aerial photographs. Malm's (1983) modeling procedure based on equation (ii) assumes that $I(o)$ and I_{sky} are independent of pollutant loading and are, therefore, constants. It is shown in the present report that this assumption is not strictly valid and that it leads to an overprediction in brightness levels, especially in the blue wavelengths.

Both the clear day and the smoggy day slides were digitized, i.e., converted into numerical form for image processing purposes. This digitization process measures the brightness level of each picture element in each of the red, green, and blue color planes which make up the photograph, and assigns a numerical density, DN, value to each point in the picture in each of the three color planes. DN values vary from 0 (black) to 255 (white) and represent the brightness level of a picture element. DN values can be related to optical density, D , values. Optical density is a measurement of light transmission through the film. From D values, the exposure, E , of the photographic slide at each point may be found using characteristic curves supplied by the film manufacturer. These exposure values are proportional to intensity values, I , and can be manipulated by using equation (ii). The extinction coefficient measured on the smoggy day is inserted into equation (ii) and is used to convert the exposure values for the clear day photo into exposure values corresponding to the smoggy day condition. The DN values corresponding to the new exposure level are found, and from this a synthetic image of the smog event can be formed. The synthetic smoggy image then is compared to the photograph taken of the actual smog event by considering both brightness and contrast levels.

The synthetic image that results from the model developed by Malm (1983) shows the contrast reduction characteristic of a smoggy day but differs from the actual image in one major respect. The synthetic photograph is too bright in all wavelengths, especially in

the blue, due to an oversimplified treatment of the sky. This dominance of blue light results in synthetic photographs with a blue cast to them. This indicates that a more accurate model should be developed. Recommendations are made for the structure of an improved calculation scheme that includes the effects of multiple scattering, ground reflection, aerosol phase function, and object reflectivity.

The visibility model also was used in a predictive capacity. The appearance of scenes in the absence of sulfates and associated water and in the absence of aerosol carbon was created. On the day modeled, greater improvement in visibility resulted from the aerosol carbon removal.

Table of Contents

	<u>Page</u>
Executive Summary	iii
List of Tables	ix
List of Figures	x
List of Photographs	xi
Acknowledgments	xii
I Introduction	1
II Experimental Program	14
III Data Analysis	25
IV Visibility Model Tested	44
V Image Processing—Approach	61
VI Results and Discussion	68
VII Conclusion	87
References	89

List of Tables

<u>Table</u>		<u>Page</u>
1	Characteristics of the Sierra Instruments Impactor	19
2	Characteristics of the Low Pressure Impactor (LPI)	20
3	Correspondence between Chemical Elements Measured and the Oxide Forms Assumed by Stelson and Seinfeld (1981)	28
4	Ion Balance—Ion Chromatography	30
5	Chemical Characterization of the Aerosol Samples	31
6	Chemical Species Contribution to the Aerosol Volume Concentration	33
7	Density and Refractive Index for Identified Species	34
8	Comparison of Aerosol Water Content Calculated by Volume Difference Method and by Sloan's Semiempirical Method	36
9	Real Part of the Volume Average Refractive Index	37
10	Comparison of Measured Scattering Coefficient to Computed Extinction Coefficient at $\lambda = 550$ nm	41
11	Components of the Extinction Coefficient	43

List of Figures

<u>Figure</u>		<u>Page</u>
1	Visibility Modeling Approach	3
2	Design for Visibility Modeling Study	4
3	Use of a Visibility Model to Predict the Effect of an Emission Control Program	6
4	Experimental Program	18
5	Aerosol Volume Distribution Observed at Pasadena, California, on April 7 and on August 25, 1983	26
6	Film Spectral Sensitivity Curves for Kodachrome 25 Slide Film	40
7	Film Characteristic Curves for Kodachrome 25 Slide Film	46
8	Geometry of Atmospheric Optics	50
9	Image Processing	73
10	Numerical Density Distributions for San Gabriel Mountains Vista	78
11	Numerical Density Distributions for Downtown Pasadena Vista	79
12	Contrast Distributions for San Gabriel Mountains Vista	80
13	Contrast Distributions for Downtown Pasadena Vista	81

List of Photographs

<u>Photograph</u>	<u>Page</u>
1 Digitized Version of Clear Day Slide (April 7, 1983) San Gabriel Mountains, gray wedge corrected	69
2 Digitized Version of Clear Day Slide (April 7, 1983) Downtown Pasadena, gray wedge corrected	69
3 Conventional Print from Slide of Actual Smog Event (August 25, 1983) San Gabriel Mountains	70
4 Conventional Print from Slide of Actual Smog Event (August 25, 1983) Downtown Pasadena	70
5 Digitized Version of Actual Smog Event (August 25, 1983) San Gabriel Mountains, gray wedge corrected	72
6 Digitized Version of Actual Smog Event (August 25, 1983) Downtown Pasadena, gray wedge corrected	72
7 Synthetic Image of Smog Event (August 25, 1983) San Gabriel Mountains	74
8 Synthetic Image of Smog Event (August 25, 1983) Downtown Pasadena	74
9 Synthetic Image of August 25, 1983, Smog Event with Removal of all Aerosol Carbon, Downtown Pasadena	83
10 Synthetic Image of August 25, 1983, Smog Event with Removal of all Sulfates and Associated Water, Downtown Pasadena	83
11 Conventional Print from Slide of Actual Clear Day (April 7, 1983) Downtown Pasadena	85
12 Digitized Version of Actual Clear Day (April 7, 1983) Downtown Pasadena, Color Enhanced to Create Perceptual Match to Conventional Color Print	85

Acknowledgments

We would like to acknowledge the many people who assisted in this project. Their help, encouragement, and dedication formed an integral part of this work.

We thank Shohreh Gharib for her patience in filter weighing and equipment preparation, Dana Brennan for her detailed work in creating the distance images, and Chris Tiller for her assistance in running some of the initial experiments.

Assistance with the chemical analysis of aerosol samples was rendered by Drs. James Huntzicker of the Oregon Graduate Center, Thomas Cahill and his staff at the Crocker Nuclear Laboratory of the University of California at Davis, and John Cooper of NEA Incorporated in Beaverton, Oregon. The South Coast Air Quality Management District provided information on gaseous pollutant concentrations.

Dr. James Huning at Caltech's Jet Propulsion Laboratory heads the research group that performed the image processing tasks incorporated into this report. He has been a great source of encouragement and support during the course of this research effort. Conversations with Drs. David Diner, Daniel McCleese, and Kenneth Castleman, all of the Jet Propulsion Laboratory in Pasadena, are gratefully acknowledged.

Theresa Fall and Nancy Tomer prepared most of the figures, and Christina Conti typed the manuscript.

We would like to make a special acknowledgment for the inspiration of this project to Richard Blackwell of JPL. This report is dedicated to his memory.

Chapter 1

Introduction

The reduction of visibility is one of the most easily perceived features of a polluted atmosphere. Particulate matter and gaseous pollutants can act to decrease visual range, lower contrast, and even alter the observed color of objects. Since the amendment of the Clean Air Act in 1977 to encourage the prevention and control of visibility impairment in national parks and wilderness areas, visibility reduction in relatively pristine locations has received considerable attention. The sparsely populated Southwest has been found to have the highest visibility in the continental United States (Trijonis and Shapland, 1979), while regions with many pollution sources and unfavorable meteorology have been shown to exhibit severe visibility problems. Husar et al. (1981) discuss trends in haziness in the eastern United States using data accumulated between 1910 and the present. They find the highest turbidities in major metropolitan areas. Denver is noted for its "brown cloud" (Sloan and Groblicki, 1981; Groblicki et al., 1981), and the smog problem in the Los Angeles area has been studied extensively (Hidy et al., 1974; White and Roberts, 1977; Cass, 1979).

The visibility problem in Los Angeles is a particularly serious one. Cass (1979) shows that of 413 days examined over the period August 1965-December 1974, approximately 100 days had a visual

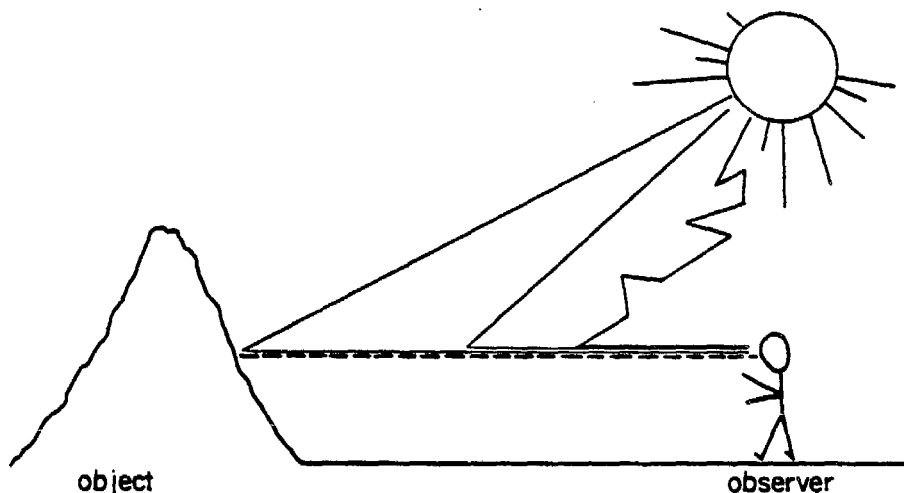
range less than three miles. In order to design air pollution abatement programs that will lead to improvement in this situation, an accurate method is needed to predict the effects on visibility of altering the air pollution profile.

The purpose of the present study is to investigate the accuracy of visibility models that generate simulated photographs as the means to display the results of the visibility model calculations. A general overview of the physical situation being modeled and the approach taken to represent this situation are given in Figure 1. A detailed description of the design for this study is shown in Figure 2. Pollutant measurements made under heavy smog conditions in Pasadena, California, are used to compute the extinction coefficient, which is a quantitative measure of the extent of light scattering and absorption in the atmosphere. The extinction coefficient value is introduced into the visibility model along with a base photograph of the scene of interest that was taken on a very clear day. Using the visibility model, the brightness and color balance of the picture elements in the base photograph are recomputed. A new synthetic image of the scene is created with the brightness and contrast expected for the conditions measured on the heavily polluted day. Color photographic prints of the synthetic smog event image are created. Then the accuracy of the visibility model can be tested by comparing the synthetic smog event image to an actual photograph taken on the heavy smog day being modeled.

Once the accuracy of a visibility model has been established,

FIGURE 1

Visibility Modeling Approach



Physical Situation : light reaching an observer includes

- light from sun to object to observer
- skylight scattered into the line of sight
- light reflected from the ground that is scattered into the line of sight

To Represent Situation

Photographically record visual appearance on clear days and on smoggy days.

Experimental Program - measure size distribution and chemical composition of atmospheric aerosol at time photographs were taken

Develop mathematical model for light scattering and absorption

Use the model and image processing techniques to produce synthetic image of the scene in presence of air pollution

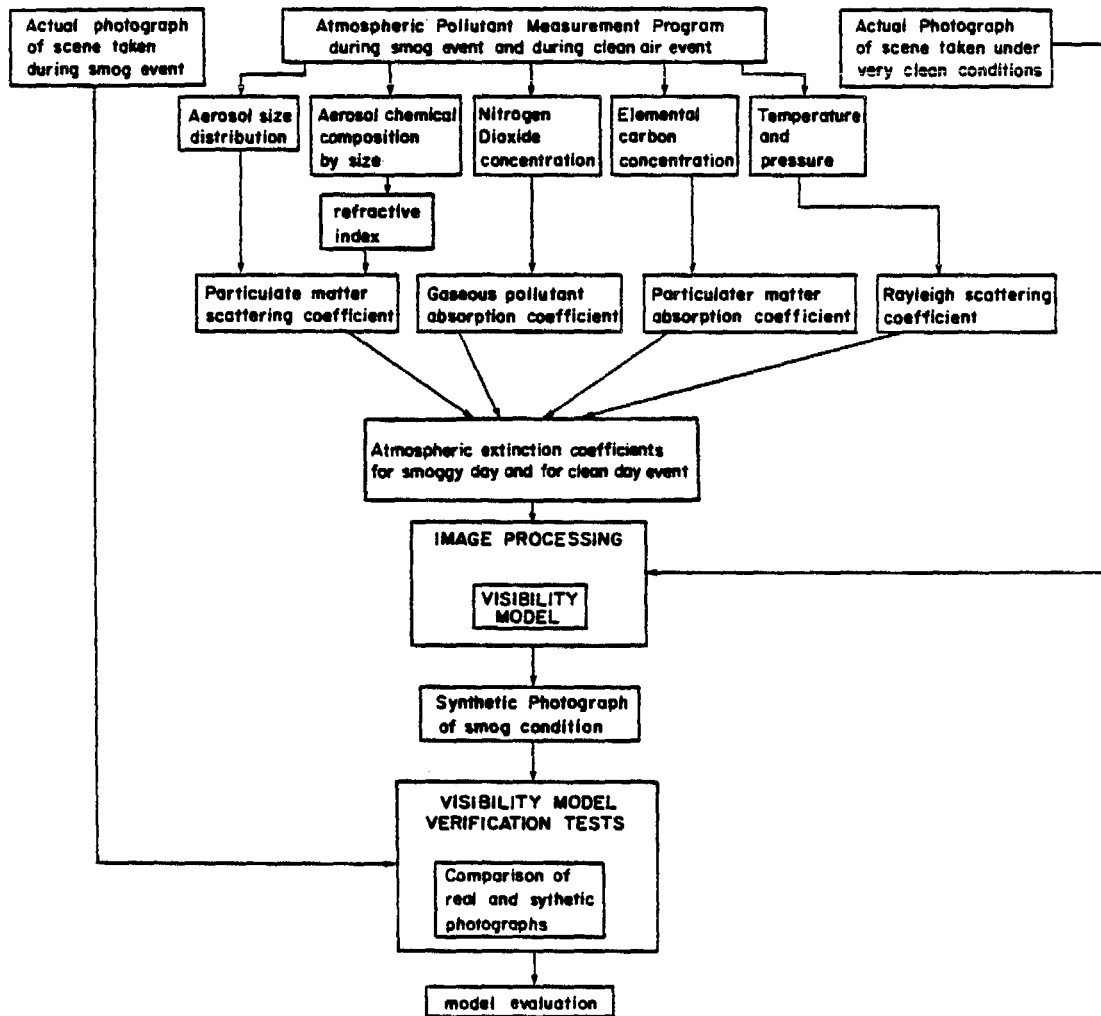
Use image processing techniques to make quantitative comparison of synthetic and actual photographs of the scene

With Procedures Verified

It is possible to construct a priori synthetic images of the scene under arbitrary pollutant loading conditions

FIGURE 2

DESIGN FOR VISIBILITY MODELING STUDY

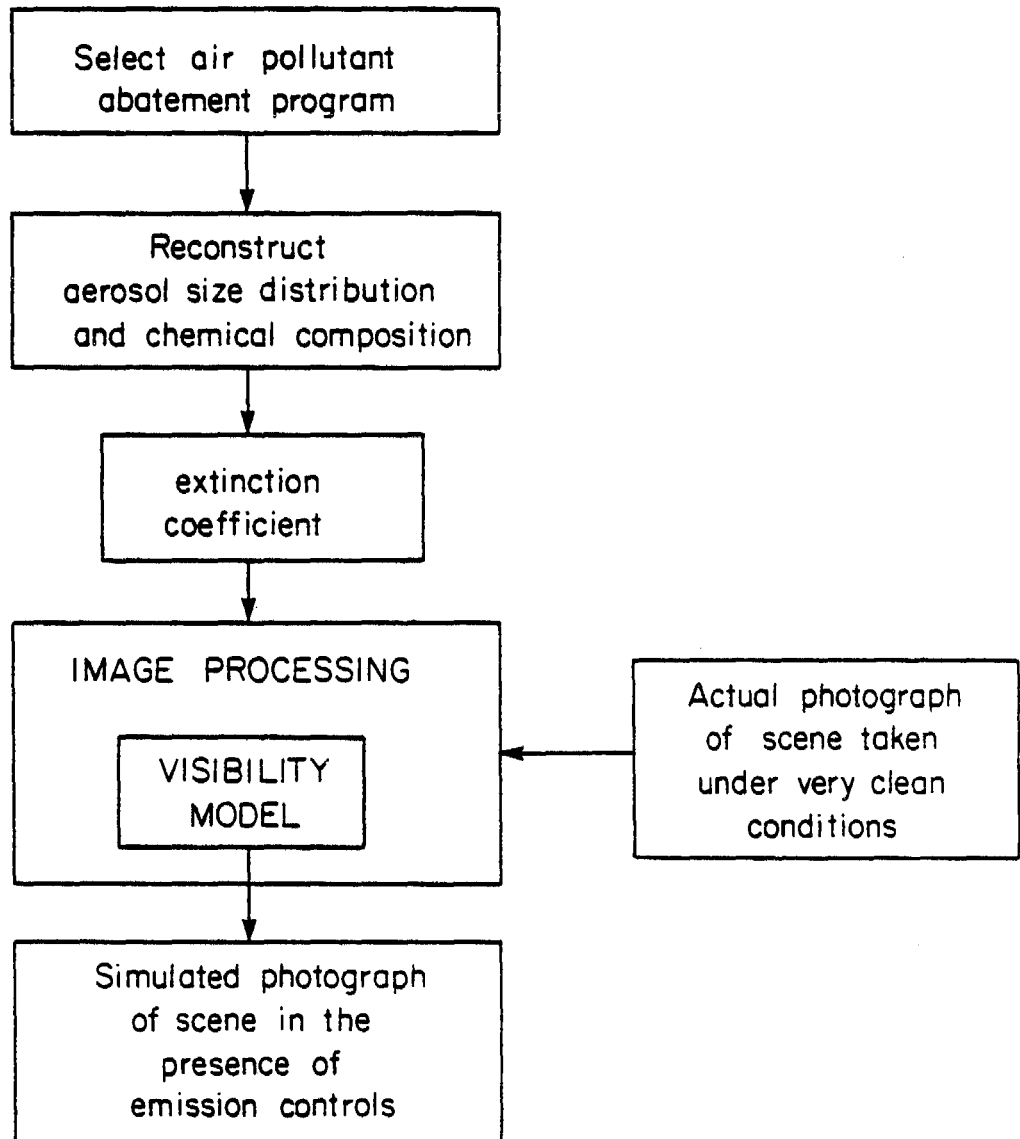


it can be used to generate a priori predictions of the appearance of a scene under arbitrary pollutant loading conditions. These predictions can be used to evaluate the effect of pollution control decisions on visibility. A verified visibility model based on image processing techniques could be used for emission control strategy evaluation as illustrated in Figure 3.

Visibility reduction is caused by scattering and absorption of light by particulate matter and by gases. Light traveling through a medium containing inhomogeneities (such as particles in the atmosphere) is subject to scattering or absorption due to the differences between the refractive indices of the medium and of the inhomogeneities. Light from the sun entering the atmosphere may travel directly to an object, where it is reflected. Before this light is viewed by an observer, some of it may be scattered out of the line of sight by pollutants in the atmosphere. This lessens the amount of information about the object that is transmitted to the observer. Light from the sky overhead can be scattered by atmospheric particles once or a multiple number of times. This scattered skylight can be redirected into the line of sight of an observer, adding to the to the brightness seen in a particular direction but carrying no information about the objects present along that line of sight. Light reflected from the ground or other objects also can be scattered into the observer's line of sight. Because the scattering and absorption efficiencies of various pollutant species (as well as object reflectivity) vary with the wavelength of light, an accurate

Figure 3

USE OF A VISIBILITY MODEL TO PREDICT THE EFFECT OF AN EMISSION CONTROL PROGRAM



description of the radiative transfer processes described above must be wavelength-dependent.

Equations of radiative transfer are essentially conservation equations. The number of different effects considered determine the complexity of these equations. For simplification, a variety of assumptions may be made, depending upon the particular case studied. One of the simplest treatments often used to describe atmospheric visibility reduction accounts only for light removed from the line of sight. Light intensity lost, dI , per path length element, ds' , is taken to be equal to the original light intensity, I , multiplied by the atmospheric extinction coefficient.

$$\frac{dI}{ds'} = -b_{\text{ext}} I \quad (1.1)$$

or

$$dI = -b_{\text{ext}} I ds' \quad (1.2)$$

where I has units of watts/steradian, s' has units of meters, and b_{ext} has units of meters⁻¹.

The extinction coefficient is a function of pollutant loading. This coefficient can be expressed as a sum of several components: light scattering by particles (b_{SCAT_p}), light absorption by particles (b_{ABS_p}), light absorption by gases (b_{ABS_g}), and light scattering by air molecules (b_{RAYLEIGH}).

$$b_{\text{ext}} = b_{\text{SCAT}_p} + b_{\text{ABS}_p} + b_{\text{ABS}_g} + b_{\text{RAYLEIGH}} \quad (1.3)$$

Integrating expression (1.2) over the path from $s' = 0$ to $s' = s$ gives

$$I = I_0 \exp(-b_{\text{ext}}s) \quad (1.4)$$

where I_0 is the original, unattenuated light intensity: the intensity at $x = 0$. This is the Lambert law of attenuation (although it was originally discovered by Bouguer around 1729). Studies have shown that humans can perceive an object as long as the contrast between the object and its background is greater than about 2% (0.02). From this contrast level and from Lambert's law, Koschmieder's formula for visual range, V_R , can be derived (Middleton, 1952):

$$V_R = \frac{-\ln 0.02}{b_{\text{ext}}} \quad (1.5)$$

$$V_R = \frac{3.9}{b_{\text{ext}}} \quad (1.6)$$

where V_R is the visual range in meters for an homogeneous atmosphere. A visibility model based on Koschmieder's formula predicts the maximum distance at which a black object viewed against the sky is barely perceptible. Such a model, though, says nothing about the quality of the appearance of objects located between the observer and the point of complete visual extinction.

Another simple visibility model accounts for light removed from the line of sight as well as for light which contains no information about the object but which is scattered into the

observer's line of sight. This light could come from sky light, ground reflection, or reflection from other objects. This model can be obtained from the basic equation of radiative transfer after making numerous simplifying assumptions.

The equation of radiative transfer is given by Chandrasekhar (1960)

$$\frac{-dI}{K\rho ds} = I - J \quad (1.7)$$

where J is the source function (in units of watts/steradian) which accounts for all light reaching the observer which did not come from the target viewed, $K\rho$ is the extinction coefficient (in units of meters⁻¹), I is the light intensity, and s is the path length. The formal solution to the equation is also given by Chandrasekhar (1960) and relates light intensity at the location of the observer, $I(s)$, to light intensity at the object viewed, $I(o)$, plus an integral term that represents light added along the line of sight.

$$I(s) = I(o)e^{-\tau(s,o)} + \int_0^s J(s')e^{-\tau(s,s')}K\rho ds' \quad (1.8)$$

where

$$\tau(s, s') = \int_{s'}^s K\rho ds \quad (1.9)$$

is the optical depth of the atmosphere between s and s' , and

$$K\rho = b_{\text{ext}} \quad (1.10)$$

If b_{ext} is assumed to be independent of distance, then the optical depth can be rewritten simply:

$$\tau(s, s') = \int_{s'}^s \kappa \rho ds \quad (1.11)$$

$$\tau(s, s') = \int_{s'}^s b_{\text{ext}} ds \quad (1.12)$$

$$\tau(s, s') = b_{\text{ext}} \int_{s'}^s ds \quad (1.13)$$

$$\tau(s, s') = b_{\text{ext}} [s - s'] \quad (1.14)$$

If $s' = 0$, then

$$\tau(s, 0) = b_{\text{ext}} s \quad (1.15)$$

Now consider the second term in equation 1.8:

$$I_{\text{path}} = \int_0^s J(s') e^{-\tau(s, s')} \kappa \rho ds' \quad (1.16)$$

Substituting equations 1.10 and 1.15 into 1.16, this becomes

$$I_{\text{path}} = \int_0^s J(s') e^{-b_{\text{ext}} s} b_{\text{ext}} ds' \quad (1.17)$$

Assuming that the source function $J(s')$ has little dependence on distance:

$$I_{\text{path}} = J \int_0^s e^{-b_{\text{ext}} s'} b_{\text{ext}} ds' \quad (1.18)$$

$$I_{\text{path}} = J \left(-e^{-b_{\text{ext}} s'} \right) \Big|_{s'=0}^{s'=s} \quad (1.19)$$

$$I_{\text{path}} = J \left(-e^{-b_{\text{ext}} s} + 1 \right) \quad (1.20)$$

$$I_{\text{path}} = J \left(1 - e^{-b_{\text{ext}} s} \right) \quad (1.21)$$

Then 1.8 is rewritten

$$I(s) = I(o)e^{-b_{\text{ext}} s} + J(1 - e^{-b_{\text{ext}} s}) \quad (1.22)$$

The assumption of horizon viewing can be used to simplify this equation. As the distance s approaches infinity (the horizon), equation 1.22 reduces to $I(\infty) = J$. This "determines" J to be the intensity of the horizon sky in the direction of the object viewed. Thus the intensity observed at a distance s from an object can be expressed as

$$I(s) = I(o)e^{-b_{\text{ext}} s} + I_{\text{sky}} (1 - e^{-b_{\text{ext}} s}) \quad (1.23)$$

The first term accounts for light from the object attenuated by the intervening atmosphere. The second term, called the path radiance, describes the light from all directions which is scattered into the line of sight.

A visibility model based on equation 1.23 can predict both intensity and contrast. Equation 1.23 also can be used as the basis for visibility models with a synthetic photograph as output. Through

computer-based image processing techniques, equation 1.23 can be applied to each picture element of a clear day base photo to convert the clear-day photograph into a synthetic smoggy-day photograph (Malm et al., 1983).

Other types of visibility models have been developed that use computer algorithms to solve the radiative transfer equation in order to model the appearance of the sky in the presence of haze or plumes. Again, image processing techniques can be used to display the output of such models (Williams et al., 1980).

Visibility models which produce synthetic photographs as an output are very attractive since they can potentially communicate a great deal of information about the quality of an observed scene in the near, mid, and far fields. Existing models of this type, though, have not been tested extensively. Before any model can be used with confidence, its predictive ability must be examined. This involves both verification of the accuracy of input data used with the model and careful quantitative comparisons between synthetic photographs and actual photographs taken of the scene and situation modeled.

The objective of the present study is to examine methods for verifying the accuracy of synthetic photograph-based visibility models using image processing techniques. An experimental program is developed to obtain valid input data on pollutant concentration, aerosol size distribution and aerosol chemical composition, and to obtain field photographs of events to be simulated. An image processing-based visibility model, derived from equation 1.23, is

tested in order to determine its accuracy and to examine procedures for visibility model verification. Deficiencies of this model are identified, and suggestions are made for improving both the model and the verification tests. Examples will be illustrated using air pollutant measurements and photographs taken in Pasadena, California, under clear day and under heavy smog conditions.

Chapter 2

Experimental Program

During the spring and summer of 1983, an experimental program was conducted to acquire observations on the size distribution and chemical composition of airborne particulate matter, as well as on gaseous pollutant concentrations in the Los Angeles area. Photographs of chosen vistas were taken simultaneously with the pollutant measurements in order to document the appearance of the air basin under different pollutant loading conditions.

One goal of the program was to collect data on an extremely clear, high-visibility day that characterizes the airshed in the near absence of air pollution. Secondly, a day was sought that displays the low summer visibility typical of the Los Angeles area. The photographs taken on the clear day can be digitized. These digitized representations of the clear day and the pollutant measurements made on the clear and smoggy days can be combined with image processing in order to degrade the clear-day image to match the high-smog event. To test the accuracy of the computer-based visibility modeling procedure, the synthetic smoggy day picture is compared to the actual photograph taken during the smog event.

The campus of the California Institute of Technology in Pasadena was chosen as the sampling site. Pasadena frequently suffers severe smog episodes during which visibility is reduced to a few

miles. The air pollutant sampling program was conducted on the roof of the Keck Laboratory building. The 144-foot-tall Millikan Library on the campus afforded unobstructed views of various scenes. Five vistas which vary in direction and character were chosen as subjects in this study. A description of the scenes follows.

Direction SW: The downtown Los Angeles area is approximately nine miles distant, and on a clear day the skyline is visible. A low ridge of hills is present along the horizon. Trees, some low-rise office buildings, and residential areas fill the foreground.

Direction NW: The view in this direction is of the downtown Pasadena area, with the city hall located in the center of the picture. Hills are along the horizon. Office buildings form much of the center of the field of view. The foreground consists of a tree-shaded parking lot.

Direction N: The San Gabriel Mountains make up the background for this scene. The midground is primarily residential. The Beckman Auditorium of the Caltech campus is in the foreground.

Direction NE: The picture is centered on Mount Wilson in the San Gabriel Mountains. The prominent features in the midground of the picture are a large church and the Pasadena City College campus.

Direction E: This direction provides a nearly endless view over Los Angeles area residential neighborhoods. The

midground contains many trees. On a very clear day, one can see the mountains adjacent to Palm Springs, a distance of approximately 135 km.

Photographs were taken using camera mounts and a tripod to ensure reproducibility of the field of view. For each scene a series of three pictures was taken using a Canon TLb, 35 mm, single-lens-reflex camera equipped with an ultraviolet light cutoff filter. Two of these pictures were taken at different f-stops to ensure proper exposure, and the third photograph incorporates a Kodak color chart for use in matching photos taken on different days. Both Kodak Ektachrome ASA 64 and Kodachrome ASA 25 have proven to be suitable films for use during the project, as both have small grain size and good color accuracy. To standardize the photographs, Kodachrome ASA 25 film was used for all the field photographs. This film has a grain size smaller than that of the ASA 64 film. Film characteristic curves and other film data are obtainable in the Kodak publication E-77, "Kodak Color Films."

Photographs were taken of each view during each air sampling event at 10 am, 12 noon, and 2 pm PST. From the five scenes and the three sets of photographs, two scenes, those of downtown Pasadena and of the San Gabriel Mountains at noon, were chosen as standard photographs for use with the visibility model. The remaining slides were archived for future work.

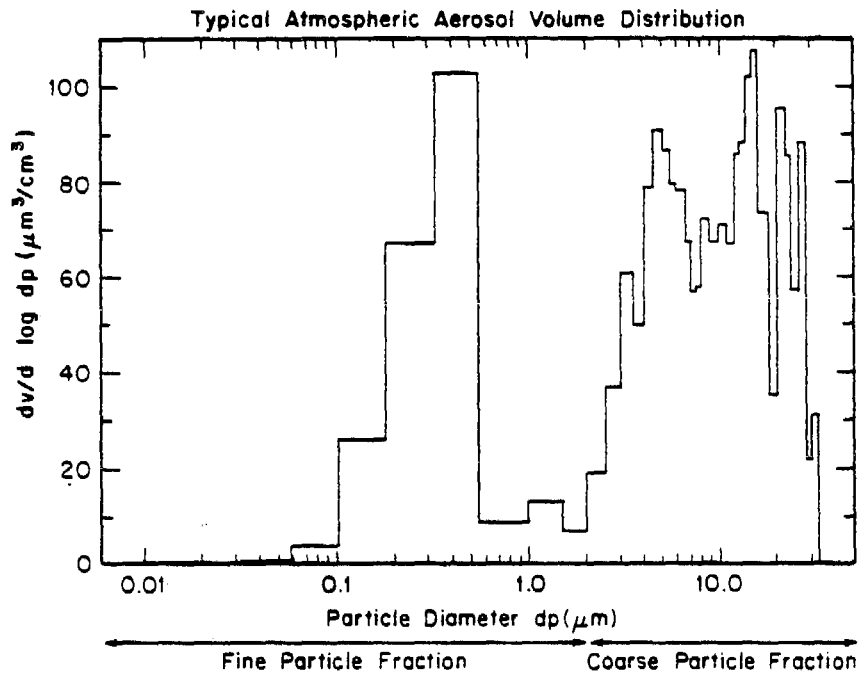
The amount of light scattered and absorbed by particulate matter is a strong function of particle size. The volume distribution

of a typical atmospheric particulate matter sample is shown in Figure 4 along with the experimental methods applied during this study to characterize the size and chemical composition of the fine particle and coarse particle fractions of this airborne material. In this study, atmospheric aerosol size distribution measurements were made using a Particle Measurement Systems model CSASP-100-HV optical particle counter (OPC) and a Thermal Systems Incorporated electrical aerosol analyzer (EAA). The OPC system senses particle size by examining light scattered by particles passing through a laser beam. Particle number concentrations can be counted within 31 particle diameter intervals ranging from 0.5 μm to 50 μm . The EAA classifies particles between 0.0075 μm and 1 μm in diameter into nine size ranges according to the particles' electrical mobility once charged.

Information on the chemical composition of the atmospheric particulate matter was obtained from several inertial impactors and from analysis of filter samples. A five-stage Marple-type impactor (Sierra Instruments model 268-KI) with a Teflon after-filter was used to collect particles on glass slides for analysis by ion chromatography. Particle bounce between impactor stages was suppressed by use of an antibounce coating (25 μl of 2% Vaseline in toluene applied 5 μl at a time to the center of each collection slide). This impactor, run at 10 lpm, separates particulate matter into stages with the following size cuts:

Figure 4

Experimental Program



Measurement Methods For
Fine Particle Fraction ($dp \leq 2.1 \mu\text{m}$)

Size Distribution:

Electrical Aerosol Analyser
Optical Particle Counter

Chemical Composition:

Marple Impactor -

ionic species by size
2 Low Pressure Impactors -
trace elements by size
elemental carbon by size

Cyclone Separator and Filters:

mass
organic carbon
elemental carbon
trace metals
 SO_4^- , NO_3^- , Cl^- , NH_4^+

Measurement Methods For
Coarse Particle Fraction ($dp \geq 2.1 \mu\text{m}$)

Size Distribution

Optical Particle Counter

Chemical Composition:

Filters:

mass
organic carbon
elemental carbon
trace metals
 SO_4^- , NO_3^- , Cl^- , NH_4^+

Other Parameters Measured:

b_{SCAT}

b_{ABS}

NO_2

Relative Humidity

Solar Radiation

Photographs Taken Of 5 Scenes At 10am, 12noon, and 2pm PST.

Table 1

Characteristics of the Sierra Instruments Impactor

Stage	Aerodynamic Cutoff Diameter (μm)
1	9.1
2	6.0
3	3.2
4	1.5
5	0.66
after filter	<0.66

Size-segregated concentration data on Na^+ , NH_4^+ , K^+ , F^- , Cl^- , NO_3^- , and SO_4^{2-} were obtained from these impactor samples by ion chromatography.

Low pressure impactors (LPI) (Hering et al., 1978, 1979) operated at 1 lpm collected aerosol samples on greased mylar substrates (1 μl of 2% Vaseline in toluene applied 0.5 μl at a time to the center of each collection slide) for chemical analysis by particle-induced x-ray emission (PIXE). The LPI, as operated, has the following size cuts when sampling dry particulate matter:

Table 2

Characteristics of the Low Pressure Impactor (LPI)

Stage	Aerodynamic Cutoff Diameter (μm)
1	4.0
2	2.0
3	1.0
4	0.5
5	0.26
6	0.12
7	0.075
8	0.05

As a further measure to prevent large particles from bouncing into the lower stages of the LPI, an AIHL-design cyclone separator (John and Reischl, 1980) was placed upstream of the LPI to remove large particles from the air stream. Air flow through the cyclone was set to pass particles with aerodynamic diameter less than 2.1 μm . Thus the upper two stages of the LPI were only lightly loaded. Analysis of the LPI samples was accomplished by cooperation with Cahill's group at the Crocker Nuclear Laboratory of the University of California at Davis. PIXE analysis yields size-segregated concentration data on 19 trace elements, ranging in atomic weight from sodium to lead. Light absorption measurements using the opal glass integrating plate technique developed by Lin et al. (1973) and modified by Ouimette (1980) also were performed on the LPI samples at Caltech to determine the distribution by size of elemental carbon.

Three sets of filters were operated downstream of the cyclone (in parallel with the LPI). These filters collected fine particle

samples. Aerosol samples collected on a Teflon filter were used to determine dry fine aerosol mass concentration by repeated weighing at low relative humidity before and after use. The concentration of 34 trace elements ranging in atomic weight from aluminum to lead was determined from the Teflon filter samples by x-ray fluorescence analysis (XRF).

Aerosol samples for light absorption coefficient determination and for ion chromatography were collected on nuclepore filters (0.4 μm diameter pore size). The aerosol light absorption coefficient, b_{ABS_p} in equation 1.3, was measured on these filter samples by the opal glass integrating plate technique. Ion chromatography provided information on the water soluble ions Na^+ , NH_4^+ , K^+ , F^- , Cl^- , S(IV) , NO_3^- , and SO_4^{2-} .

Quartz filters were used to collect samples for determination of organic and elemental carbon concentration. The carbon analysis was carried out by Dr. James Huntzicker at the Oregon Graduate Center.

A comparable set of open-faced filters was used to collect total suspended particulate matter samples. The total aerosol Teflon, nuclepore, and quartz filters were analyzed in the same manner as the fine aerosol filters. Information on the atmospheric coarse particle fraction then was determined by difference between the total and fine particle concentration data.

Care was taken in both sample preparation and sample collection not to contaminate filters or impactor substrates. Before sampling, all impactor substrates were cleaned with methanol and

toluene and subsequently greased with a 2%-by-weight solution of Vaseline in toluene. All filters were handled only with the use of clean tweezers. Quartz filters were baked prior to use at 600°C for two hours in order to drive off volatile contaminants. The quartz filters were stored, both before and after sampling, in foil-lined petri dishes to protect the filters from hydrocarbon contamination which could result from direct contact with a plastic storage dish. After sampling, all samples were placed in petri dishes, sealed, and refrigerated to minimize the possibility of chemical reaction. In addition, the cyclone, filter holders and impactors were cleaned thoroughly to eliminate these equipment items as sources of contamination.

The aerosol scattering coefficient, b_{SCAT_p} in equation 1.3, was measured during sampling using a Meteorology Research Incorporated 1550 integrating nephelometer. Relative humidity and temperature data were obtained with a sling psychrometer. Information on NO₂ gaseous pollutant concentrations was obtained from the South Coast Air Quality Management District's Pasadena monitoring station. That SCAQMD station is located on the Caltech campus and thus is in very close proximity to the particulate sampling site.

Over the period from October 28, 1982, through August 25, 1983, 15 sampling days were selected. From these experiments, three sets of filter and impactor samples were chosen for complete chemical analysis. A very clear day event was studied on April 7, 1983, when strong Santa Ana conditions prevailed in the Los Angeles basin,

resulting in a visual range of approximately 60 miles. The measured scattering coefficient averaged approximately $0.4 \times 10^{-4} \text{ m}^{-1}$ over that day. The Rayleigh limit for scattering by air molecules in the absence of any air pollution is $0.23 \times 10^{-4} \text{ m}^{-1}$ at a wavelength of 550 nm, indicating that the April 7, 1983, samples come very close to representing the Pasadena area in the absence of air pollutants.

A heavy smog situation was studied on May 24, 1983. In this case visual range was reduced to less than 3 miles. The average measured scattering coefficient for this day was $7 \times 10^{-4} \text{ m}^{-1}$. Further analysis showed that modeling this smog episode would be difficult. Although the relative humidity was only 55%, the aerosol seemed to show a great deal of water retention, most likely the result of a hysteresis effect. Determining how water is associated with atmospheric particulate matter over the size range of interest is a difficult problem.

Samples collected on August 25, 1983, also were chosen for further analysis. The average scattering coefficient measured was approximately $5 \times 10^{-4} \text{ m}^{-1}$. The visual range was about 5 miles. It was decided that the data from the April 7th and the August 25th days would be used in the model verification study. Shadow patterns in the photographs taken on these two days are nearly identical since these days are almost symmetrically spaced on either side of the summer solstice.

Data collected from these experiments first were used to calculate the volume averaged refractive index for the aerosol present

on the two days studied. Then the refractive index and size distribution data were combined with Mie scattering and absorption calculations to compute the atmospheric extinction coefficient. Those extinction coefficient values are the principal link between the air pollution problem and the visibility model calculations. The next section of this report discusses the results of the data analysis and the calculation of the extinction coefficient.

Chapter 3

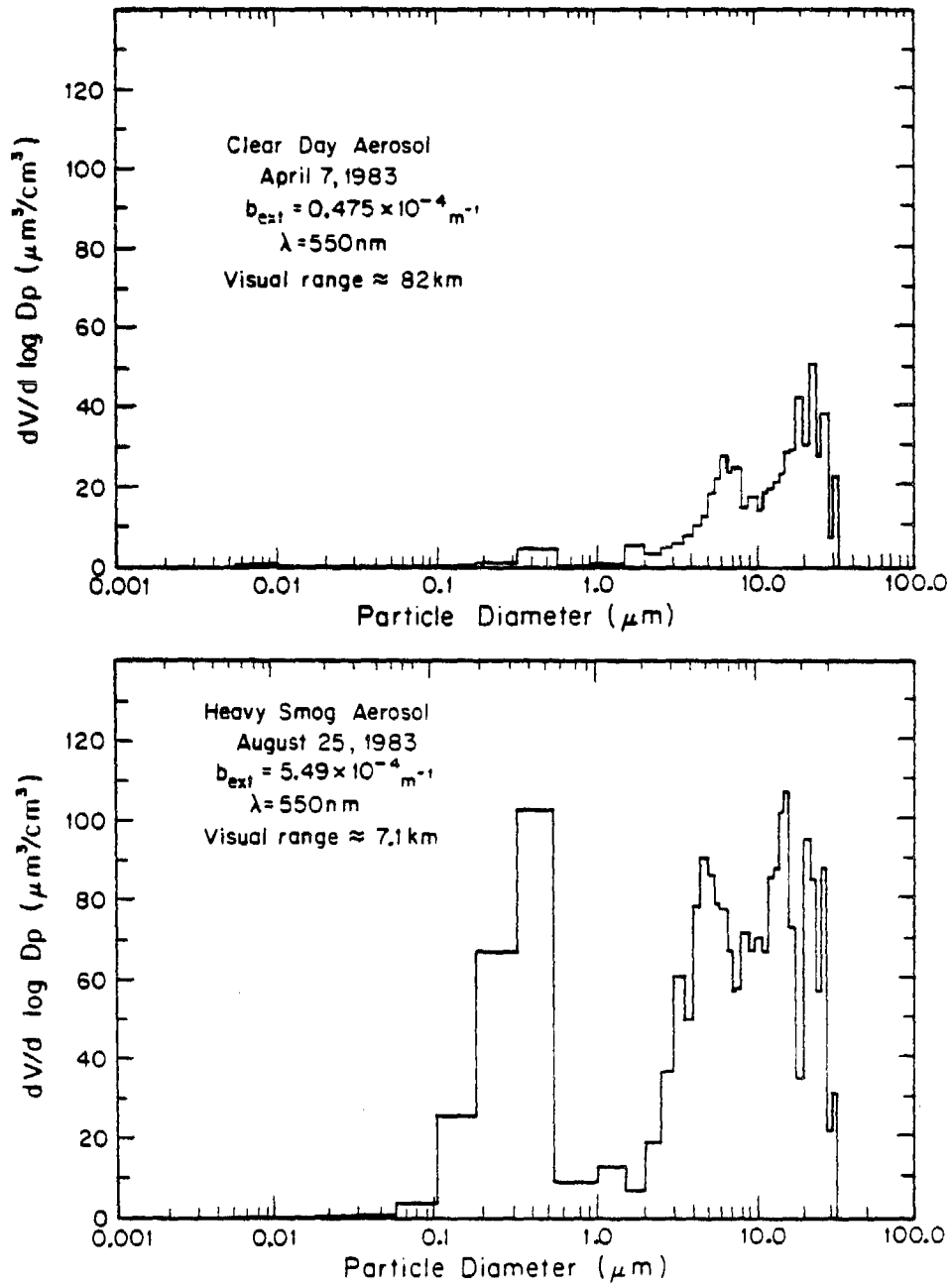
Data Analysis

Light scattering by airborne particles is a strong function of particle size. The size distributions of the atmospheric aerosol present on the clear day and on the heavy smog day were determined by combining the measurements made by the optical particle counter (OPC) and by the electrical aerosol analyzer (EAA). The EAA and OPC can provide nearly continuous readings of the size distribution over the course of an experiment. OPC size distribution data, recorded at 5- to 15-minute intervals, and EAA size distribution information, taken at one-half to one-hour intervals, were averaged within each size cut (or channel) over the same span of time that the filter and impactor sampling occurred. EAA data were used for particle diameters less than $0.75 \mu\text{m}$. The OPC data were used for diameters larger than $0.75 \mu\text{m}$. The size distribution gives the number concentration of particles present in each size range. From this information, the volume of particles in each size range can be determined.

Figure 5 shows the volume distribution of the atmospheric aerosol on the clear day (April 7, 1983) and on the heavy smog day (August 25, 1983). The usual bimodal nature of the volume distribution is evident. Particles in the fine mode ($d_p < 2 \mu\text{m}$) are much more efficient light scatterers than are the coarse particles. An appreciable difference in the fine modes on the two days can be seen easily from the graphs. This difference is the main cause for

Figure 5

AEROSOL VOLUME DISTRIBUTION OBSERVED AT
PASADENA, CA. ON APRIL 7 AND ON AUGUST 25, 1983



the large difference in the extinction coefficient, and therefore in the visual range, on the two days shown.

In order to estimate the refractive index of the fine and coarse airborne particulate matter, information on chemical composition as a function of particle size is required. Several measurements (by differing methods) were made of certain aerosol properties. Wherever possible, these duplicate measurements were used to perform consistency checks on the data.

The procedure of Stelson and Seinfeld (1981) was adopted for preparing a material balance on the chemical composition of the aerosol samples. The balance describes the contribution of major chemical species to the total dry particle mass present in the aerosol phase during the two days of interest. Stelson and Seinfeld show that for the Los Angeles area, aerosol mass can be described from measurements of SO_4^{-2} , Cl^- , Br^- , NO_3^- , NH_4^+ , Na^+ , K^+ , Ca^{+2} , Fe, Mg, Al, Si, Pb, carbonaceous material and aerosol water. Their method assumes that trace metals are present in the form of common oxides, as shown in Table 3. In the present study, the elements measured are assumed to have the chemical forms given in Table 3, with the exception of Na. As will be discussed, Na was assumed to be in the form of an ionic solid. Mg was present at negligible concentrations during the present experiment, and thus its chemical form is unimportant to the aerosol mass balance. In order to account for hydrogen and oxygen present in the hydrocarbons, the mass of organic carbonaceous material was taken to be 1.2 times the organic carbon mass measured (Countess et al.,

TABLE 3

Correspondence Between Chemical Elements
Measured and the Oxide Forms
Assumed by Stelson and Seinfeld (1981)

element	oxide form
Al	Al_2O_3
Ca	CaO
Fe	Fe_2O_3
Si	SiO_2
Mg	MgO
Pb	PbO
Na	Na_2O
K	K_2O

1980). The ionic material was assumed to be distributed as follows. (Major ions measured were Na^+ , NH_4^+ , K^+ , SO_4^{-2} , NO_3^- , and Cl^- .)

Na^+ was associated with Cl^- .

NH_4^+ was associated with SO_4^{-2} .

NH_4^+ remaining, if any, was associated with NO_3^- .

Na^+ remaining, if any, was associated with remaining NO_3^- , if any.

Na^+ remaining, if any, was associated with remaining SO_4^{-2} , if any.

Results of an ionic species balance on the water soluble portion of the aerosol for the two days investigated are presented in Table 4. The ion balance on the smoggy day (August 25th) is quite good. The amount of material present in the clean day (April 7th) samples was near the minimum detection level of the ion chromatograph used. These very low levels account for the higher percentage errors in the ion balance that day. Some of that discrepancy also may be explained if ions are present that cannot be identified by ion chromatography using the columns which were available during this study. Ions other than those listed above were assumed to be minor contributors to total mass.

The final chemical characterization of fine and coarse particle material measured on the two days of interest is shown in Table 5. The summation of the mass concentrations of the individual chemical species gives a total dry aerosol mass concentration. This calculated concentration is compared to the measured aerosol mass concentration. The measured concentration is determined gravimetrically from each Teflon filter by repeated before and after weighing of the filters at low relative humidity.

TABLE 4
ION BALANCE
ION CHROMATOGRAPHY

APRIL 7, 1983

FINE FILTER				TOTAL FILTER			
Measured Anions	Conc. ($\mu\text{eq}/\text{m}^3$)	Measured Cations	Conc. ($\mu\text{eq}/\text{m}^3$)	Measured Anions	Conc. ($\mu\text{eq}/\text{m}^3$)	Measured Cations	Conc. ($\mu\text{eq}/\text{m}^3$)
F ⁻¹	1.05×10^{-3}	Na ⁺¹	*	F ⁻¹	1.18×10^{-3}	Na ⁺¹	8.06×10^{-2}
Cl ⁻¹	5.59×10^{-3}	NH ₄ ⁺¹	*	Cl ⁻¹	1.27×10^{-2}	NH ₄ ⁺¹	9.20×10^{-2}
NO ₃ ⁻¹	8.98×10^{-3}	K ⁺¹	*	NO ₃ ⁻¹	1.54×10^{-2}	K ⁺¹	*
SO ₄ ⁻²	4.96×10^{-2}			SO ₄ ⁻²	5.37×10^{-2}		
TOTAL	6.52×10^{-2}	TOTAL	*	TOTAL	8.30×10^{-2}	TOTAL	1.73×10^{-1}

AUGUST 25, 1983

FINE FILTER				TOTAL FILTER			
Measured Anions	Conc. ($\mu\text{eq}/\text{m}^3$)	Measured Cations	Conc. ($\mu\text{eq}/\text{m}^3$)	Measured Anions	Conc. ($\mu\text{eq}/\text{m}^3$)	Measured Cations	Conc. ($\mu\text{eq}/\text{m}^3$)
F ⁻¹	*	Na ⁺¹	1.54×10^{-1}	F ⁻¹	*	Na ⁺¹	2.04×10^{-1}
Cl ⁻¹	4.42×10^{-2}	NH ₄ ⁺¹	1.18×10^{-1}	Cl ⁻¹	7.28×10^{-2}	NH ₄ ⁺¹	2.48×10^{-1}
NO ₃ ⁻¹	3.81×10^{-2}	K ⁺¹	*	NO ₃ ⁻¹	1.73×10^{-1}	K ⁺¹	*
SO ₄ ⁻²	2.25×10^{-1}			SO ₄ ⁻²	2.26×10^{-1}		
TOTAL	3.07×10^{-1}	TOTAL	3.35×10^{-1}	TOTAL	4.72×10^{-1}	TOTAL	4.52×10^{-1}

NOTE: Concentrations are given in units of microequivalent per m³ of air.

* below minimum detection levels

TABLE 5

Chemical Characterization of the Aerosol Samples

	<u>April 7, 1983</u>		<u>August 25, 1983</u>	
	Fine $\frac{\mu\text{g}}{\text{m}^3}$	Coarse $\frac{\mu\text{g}}{\text{m}^3}$	Fine $\frac{\mu\text{g}}{\text{m}^3}$	Coarse $\frac{\mu\text{g}}{\text{m}^3}$
$(\text{NH}_4)_2\text{SO}_4$	3.28	0.26	11.94	2.96
NH_4NO_3	0.72	0.51	-	1.79
NaNO_3	-	-	3.24	9.56
Na_2SO_4	-	-	3.12	-
elemental carbon	0.59	0.40	7.97	-
organic carbon	5.59	1.19	28.14	4.60
Al_2O_3	0.52	2.30	1.76	7.58
SiO_2	0.68	3.85	1.94	13.60
K_2O	0.063	0.30	0.45	1.00
CaO	0.076	0.37	0.23	1.60
Fe_2O_3	0.14	0.77	0.70	3.88
PbO	0.058	0.002	0.62	0.10
other metals and ionic species	0.49	2.50	3.13	1.80
Total Material Identified by Chemical Analysis	12.21	12.45	63.24	48.47
Mass Concentration Measured Gravimetrically	10.00	12.71	87.28	59.29
Percent of Gravimetrically Determined Mass by Chemical Analysis	122%	98%	72%	82%

This method accounted for all of the dry mass on the clean day (to within accumulated measurement uncertainties) and 76% of the total mass on the heavy smog day (August 25, 1983). The mass unaccounted for could have been due to material that is not identified by the chemical analysis procedures used, to water adsorbed onto the Teflon filters during the weighing procedure despite desiccation, or to departure from baseline assumptions about the oxygen content of the samples. It will be assumed that the unidentified aerosol mass on August 25 was due to unmeasured chemical species.

A balance on the chemical species contribution to fine and coarse aerosol volume is shown in Table 6. Densities for individual chemical species were assigned as shown in Table 7. The mass of dry material that was not associated with a particular chemical compound via chemical analysis, the "residue," was assigned a density of 2.3 g/cm^3 (Sloan, 1983). Using the individual densities and the measured masses of individual chemical constituents, a dry volume is calculated. The sum of volumes for each species gives the total volume that the aerosol would occupy if no water were present in the aerosol. When this dry aerosol volume is subtracted from the total aerosol volume computed from the size distribution measurements of the EAA and OPC, one estimate of the volume of water present in the aerosol is obtained. For comparison, the semiempirical procedure for estimating aerosol water content formulated by Sloan (1983) was applied to the Pasadena aerosol measurements. In this approach, data on ambient relative humidity and the aerosol solubility are used to estimate the amount of water present in the aerosol. The results of

TABLE 6

Chemical Species Contribution to
the Aerosol Volume Concentration

Date	April 7, 1983		August 25, 1983	
	Particle Fraction		Particle Fraction	
Species	Fine	Coarse	Fine	Coarse
	volume conc. $\frac{\mu\text{m}^3}{\text{cm}^3}$	volume conc. $\frac{\mu\text{m}^3}{\text{cm}^3}$	volume conc. $\frac{\mu\text{m}^3}{\text{cm}^3}$	volume conc. $\frac{\mu\text{m}^3}{\text{cm}^3}$
elemental carbon	0.295	0.200	3.985	0
organic carbon	3.993	0.850	20.10	3.286
$(\text{NH}_4)_2\text{SO}_4$	1.853	0.147	6.734	1.672
NaNO_3	-	-	1.434	4.230
NH_4NO_3	0.419	0.297	-	1.041
Na_2SO_4	-	-	1.164	-
other ions	0.095	1.087	0.965	0.552
Al_2O_3	0.131	0.580	0.444	1.914
SiO_2	0.296	1.674	0.843	5.913
K_2O	0.027	0.128	0.194	0.431
CaO	0.023	0.115	0.071	0.492
Fe_2O_3	0.027	0.147	0.134	0.740
PbO	0.007	2.5×10^{-4}	0.078	0.013
other metals	0.113	-	0.396	0.230
Total Dry Volume of Identified Chemical Species	7.279	5.220	36.54	20.515
Volume of Residue*	0.00	0.130	10.45	6.76
(2) Total Dry Volume	7.279	5.350	46.99	27.28
(1) Volume From Size Distribution	2.333	23.534	56.52	82.43
Volume H_2O [by (1)-(2)]	0.00	18.18	9.53	55.15

* Residue is defined as material identified gravimetrically that is not identified chemically; assumed to have a density of 2.3 g/cm^3 .

TABLE 7

Density and Refractive Index Values
for Selected Chemical Species

<u>species</u>	<u>density</u> <u>(g/cm³)</u>	<u>refractive</u> <u>index</u>	<u>reference</u>
elemental carbon	2.0	1.90-0.6i	1
organic carbon	1.40	1.55	1
(NH ₄) ₂ SO ₄	1.77	1.52	2
NaNO ₃	2.26	1.59	2
NH ₄ NO ₃	1.72	1.55	1,2
Na ₂ SO ₄	2.68	1.48	2
other ions	2.30	1.53-0.005i	1
Al ₂ O ₃	3.96	1.76	2
SiO ₂	2.30	1.48	2
K ₂ O	2.32	1.50	2
CaO	3.25	1.84	2
Fe ₂ O ₃	5.24	3.01	2
PbO	8.00	2.61	2
other materials	2.30	1.53-0.005i	1
water	1.00	1.33	2

References:

- 1) Sloan (1983)
- 2) Handbook of Chemistry and Physics (1975-1976)

this calculation are presented in Table 8. These two approaches to estimating the amount of water present provide virtually identical answers for the fine aerosol fractions. The disagreement shown for the water content of coarse particle material is unimportant to subsequent visibility calculations: coarse particles by virtue of their size contribute only a small fraction to total aerosol light scattering.

Once the contributions to the aerosol volume from individual pollutants and from associated liquid water have been determined, it is possible to determine a volume average refractive index for the aerosol. The volume average refractive index for both coarse particle and fine particle modes is shown in Table 9. Kerker (1969) discusses the validity of the volume average refractive index. He finds the volume averaged index to be within approximately 20% of the exact refractive index for a typical internally mixed aerosol particle.

Using the aerosol size distribution and the volume averaged refractive indices for the coarse particle and fine particle modes, it is possible to compute the extinction coefficient for the aerosol. The computer algorithm used is a Mie scattering code as outlined by Wickramasinghe (1973). Mie's solution describes light scattered by a homogenous sphere in an infinite medium, determining the scattering efficiency factor, Q_{SCAT} (no units). Q_{SCAT} is the ratio of the scattering cross section to the particle geometric cross section. The scattering cross section is "that cross section of an incident wave, acted on by the particle, having an area such that the power flowing across it is equal to the total power scattered in all directions" by

TABLE 8

Comparison of Aerosol Water Content Calculated
by Volume Difference Method and
by Sloan's Semiempirical Method

Date	April 7, 1983		August 25, 1983	
<u>Particle Fraction</u>	<u>Fine</u>	<u>Coarse</u>	<u>Fine</u>	<u>Coarse</u>
volume H ₂ O by difference ($\mu\text{m}^3/\text{cm}^3$)	0.00	18.18	9.53	55.15
volume H ₂ O by Sloan's method ($\mu\text{m}^3/\text{cm}^3$)	0.26	0.34	11.86	11.16

TABLE 9

Real Part of the Volume
Average Refractive Index

Date	April 7, 1983		August 25, 1983	
<u>Particle Fraction</u>	<u>Fine</u>	<u>Coarse</u>	<u>Fine</u>	<u>Coarse</u>
Refractive Index	1.56	1.39	1.54	1.42
Refractive Index with all Aerosol Sulfate and Associated Water Removed			1.49	1.42
Refractive Index with all Aerosol Carbon Removed			1.48	1.41

the particle (McCartney, 1976). Q_{SCAT} depends on particle size, refractive index, and light wavelength. For a monodisperse aerosol, the scattering coefficient is related to the scattering efficiency by

$$b_{\text{SCAT}_p} = N \frac{\pi}{4} d_p^2 Q_{\text{SCAT}_p} \quad (3.1)$$

where N is the number of particles per unit volume and d_p is the particle diameter. For a polydisperse aerosol b_{SCAT_p} can be expressed

as

$$b_{\text{SCAT}_p} = \int_0^{\infty} Q_{\text{SCAT}_p} \frac{\pi}{4} d_p^2 n(d_p) d(d_p) \quad (3.2)$$

where $n(d_p)d(d_p)$ is the number of particles per unit air volume with diameter between d_p and $d_p + d(d_p)$. For a measured aerosol size distribution, in histogram form, the integral is approximated by a sum:

$$b_{\text{SCAT}_p} = \sum_{i=1}^m Q_{\text{SCAT}_p} \frac{\pi}{4} d_{p_i}^2 N(d_{p_i}) \quad (3.3)$$

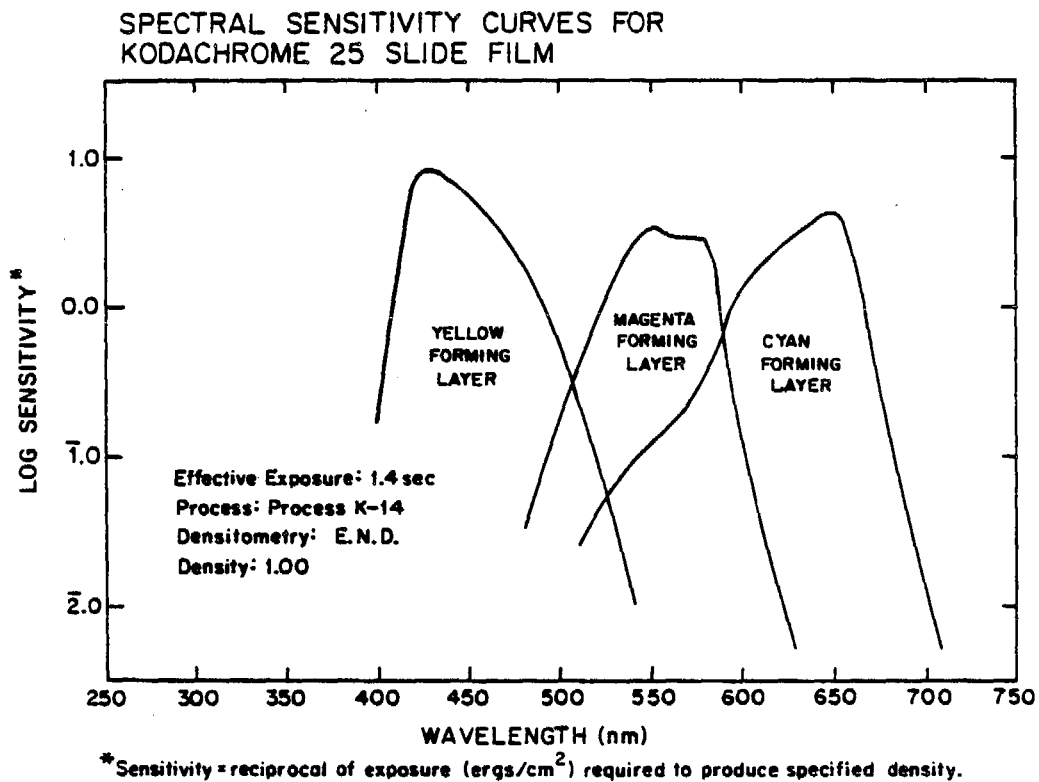
where the d_{p_i} represent the central points of successive diameter intervals, d_{p_1} is the smallest diameter interval, and d_{p_m} is the largest diameter interval for which number concentration information is available.

Equation (3.3) was applied to calculate the scattering coefficient of the aerosol observed on April 7 and on August 25, 1983.

Separate refractive index values were used for coarse particle and for fine particle modes of the aerosol volume distribution, as outlined in Table 9. The refractive index is assumed constant over the visible spectrum (Nicholls, 1984). Color photographic slides can be separated into three different color planes: red, green, and blue. The superposition of these planes creates a full color image. The Kodachrome ASA 25 film used to produce the slides taken in the field has a wavelength sensitivity profile as shown in Figure 6. The yellow-forming layer is blue-sensitive; the magenta-forming layer is green-sensitive; and the cyan-forming layer is red-sensitive. To incorporate this color sensitivity into the model, the scattering coefficient was calculated at each of 13 different wavelengths within the visible spectrum, and these values were weighted according to the film sensitivity curves. This results in three values of a weighted average scattering coefficient, one corresponding to each color plane. The weighted green value should most closely match the scattering coefficient value measured by the nephelometer during the field experiments. The measured and computed scattering coefficient values agree within 20% (Table 10).

Equation 1.3 shows that light absorption by aerosols and gases, plus light scattering by air molecules, must be added to the aerosol scattering coefficient in order to estimate the total atmospheric extinction coefficient. The particle absorption coefficient, b_{ABS_p} , (due to elemental carbon) was measured using the opal glass integrating plate technique (Lin et al., 1973, as modified

FIGURE 6



© Eastman Kodak Company, 1980.
Reprinted courtesy of Eastman Kodak Company.

Table 10

Comparison of Measured Scattering
Coefficient to Computed
Extinction Coefficient at $\lambda=550\text{nm}$

	Clear Day Aerosol (April 7, 1983)	Heavy Smog Aerosol (August 25, 1983)
b_{SCAT_p} -Calculated ($\times 10^{-4} \text{m}^{-1}$)	0.259	4.08
b_{ABS_p} ($\times 10^{-4} \text{m}^{-1}$) due to elemental carbon	0.093	0.787
b_{Rayleigh} ($\times 10^{-4} \text{m}^{-1}$)	0.111	0.107
b_{ABS_g} ($\times 10^{-4} \text{m}^{-1}$) due to NO_2	0.0118	0.0299
b_{ext} -Calculated ($\times 10^{-4} \text{m}^{-1}$)	0.475	5.00
b_{SCAT} Measured ($\times 10^{-4} \text{m}^{-1}$)	0.29	5.1

by Ouimette, 1980). The principal light absorbing gas in urban atmospheres is NO_2 . The wavelength dependence of this absorption is discussed by Dixon (1940). The results of his study were put in a more practical form by R. J. Hodkinson (1966) (Groblicki et al., 1981). Using this dependence, the weighted average gaseous absorption coefficients, b_{ABS_g} , (for the red, blue, and green wavelength bands) were determined.

Light scattering by air molecules, Rayleigh scattering, has been studied extensively. Penndorf (1957) presents tables of the Rayleigh scattering coefficient for standard air over a wide band of wavelengths, including the visible. He points out that Rayleigh scattering is temperature-dependent and that this dependence cannot be ignored. These tables and Penndorf's temperature correction formula were used to determine the weighted averages for the Rayleigh scattering coefficients in the red, green, and blue.

The individual components of the extinction coefficient and their sum are shown for the two days of interest in Table 11.

TABLE 11

Components of the
Extinction Coefficient

(units are 10^{-4} m^{-1})

DATE	COLOR PLANE	b_{SCAT_p}	b_{ABS_p}	b_{ABS_g}	b_{RAY}	b_{ext}
April 7	blue	0.305	0.0930	0.0541	0.281	0.733
	green	0.259	0.0930	0.0118	0.111	0.475
	red	0.231	0.0930	0.00278	0.0659	0.393
Aug. 25	blue	5.56	0.787	0.136	0.273	6.76
	green	4.08	0.787	0.0299	0.107	5.00
	red	3.52	0.787	0.00694	0.0639	4.38
Aug. 25 minus sulfates	blue	5.30	0.787	0.136	0.273	6.50
	green	3.92	0.787	0.0299	0.107	4.84
	red	3.08	0.787	0.00694	0.0639	3.94
Aug. 25 minus carbon	blue	2.81	0.0	0.136	0.273	3.22
	green	1.96	0.0	0.0299	0.107	2.10
	red	1.68	0.0	0.00694	0.0639	1.75

Chapter 4

Visibility Model Tested

A relatively uncomplicated visibility model for use with synthetic image processing techniques has been proposed by Malm (1983). Malm applied that modeling approach to generate synthetic images under hypothetical air pollutant loading conditions, but the model has yet to be tested for its accuracy in reproducing the appearance of an actual smog episode. In this chapter, the accuracy of Malm's modeling approach will be examined.

The instructions for use of Malm's model are as follows. The model is essentially an application of equation 1.23 in radiance form:

$$N(s) = N(o)e^{-b_{ext}s} + N_{sky} (1 - e^{-b_{ext}s}) \quad (4.1)$$

Radiance (in units of watts per square meter per steradian, $W m^{-2} sr^{-1}$) describes the radiant flux leaving an extended surface. It is defined as "the ratio of the radiant flux leaving an element of the surface to the product of the projected area of the element and solid angle as each of these two quantities are made indefinitely small" (McCartney, 1976). For Lambertian surfaces (a surface which reflects light equally in all directions), the radiance is the intensity of the object per unit surface area. In equation 4.1, $N(s)$ is the radiance of an object at distance s from the object. $N(o)$ is the "inherent radiance," the radiance of an object at the object. N_{sky} is the radiance of the sky in the direction viewed. In order

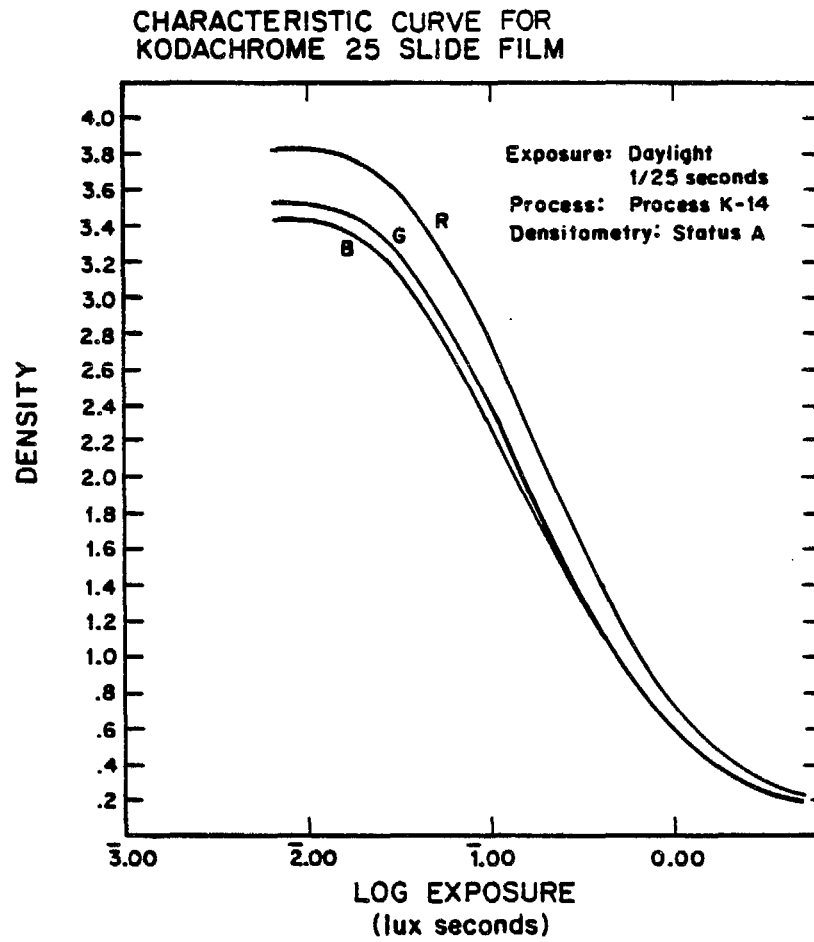
to produce a synthetic picture output, this equation must somehow be applied to alter the digital representation of a color photograph. An actual 35 mm slide of the scene of interest taken on a clear day is scanned by a microdensitometer in order to subdivide it into a matrix of picture elements, called pixels. The microdensitometer scans the photo in three separate wavelength bands, creating three color-separated images in the red, green, and blue color planes. The relationship between film density (which is related to the transparency of the exposed film at a particular wavelength and which can be measured by a densitometer) and exposure (which can be related to the radiance reaching the film as the picture was taken) is given in the "D vs. E" characteristic curves provided by the film manufacturer. The D vs. E curves for Kodak ASA 25 slide film are shown in Figure 7 (Kodak Color Films, 1980). Thus the film can be used as a light-measuring device, and the clear day color slide can be converted to an array of $N(s)$ values at three wavelengths giving the radiance of each object in the field of view.

From that array of clear day $N(s)$ values, Malm next back-calculated the inherent radiance of the objects at each point in the clear day picture by rearranging equation 4.1, giving

$$N(o) = N(s) e^{b_{ext}s} + N_{sky} (1 - e^{b_{ext}s}) \quad (4.2)$$

The horizon sky radiance, N_{sky} , was obtained by evaluating the film densities at locations along the horizon on the clear day image. For objects below the horizon, the approximation of horizon viewing was still assumed to be valid, and N_{sky} values were determined using an

FIGURE 7



© Eastman Kodak Company, 1980. Reprinted courtesy of Eastman Kodak Co.

extrapolation of sky brightness trends to below the horizon. In Malm's study, the extinction coefficient for the atmosphere at the time that the clear day photograph was taken was assumed to be known but was not measured. Distances, s , to objects in the field of view were assigned using topographic maps.

The assumption is then made that the inherent radiance, $N(o)$, and the sky radiance values, N_{sky} , are independent of atmospheric pollutant loading. Therefore, $N(o)$ and N_{sky} for every object in any pollution condition are now known. The distance from object to observer also has been determined. In order to simulate a smoggy day, one must only set b_{ext} in 4.1 at the proper level and then determine a new radiance for each object. This produces an array of new $N(s)$ values that correspond to the smog event to be simulated. This new array can be related to a new, synthetic film density array which is used to create a new image. The calculation is done for each picture element in each of the three color planes. Superposing these planes results in a synthetic image that can be played back onto photographic film using a film-writing device. A color negative results, from which color prints can be made.

In order to determine if this image processing procedure is a valid method for reproducing the appearance of low visibility events, Malm's approach was tested against data taken during the 1983 field experiments in Pasadena, California. The following revisions to Malm's approach were made in order to facilitate this test.

- (1) The extinction coefficient would be determined from measured aerosol and gaseous pollutant properties, not by estimation. Wavelength dependences would be carefully accounted for. The film sensitivity as a function of wavelength would be considered.
- (2) High resolution in the synthetic image would be sought. This implies a small pixel size.
- (3) A detailed distance image would be created so that the model's sensitivity to distance largely would be eliminated as a source of uncertainty.
- (4) Field photographs would be taken under the same conditions as those modeled.
- (5) Field photographs and synthetic photographs would be compared using quantitative numerical tests.

On the hypothesis that comparison of synthetic and actual photographs of a heavy smog event might not match in all respects, a better understanding was sought of the possible failings of a visibility model based on equations 4.1 and 4.2.* In order to describe the process of radiative transfer more fully than in equation 4.1, it is necessary first to define several variables and to make an assumption about atmospheric structure. It is assumed that atmospheric properties are only functions of height. The variation is

*In the following, the discussions with Dr. David Diner of the Jet Propulsion Laboratory in Pasadena, California, are gratefully acknowledged.

only vertical, not horizontal. Referring to Figure 8, the variables needed are

r = reflectivity of object,
assumed Lambertian (i.e.,
radiation is reflected equally
in all directions) (no units)

x_0 = distance from object to the
top of the atmosphere (in
units of meters)

τ = optical depth at object (no
units), $\tau = \int_{x=0}^{x=x_0} b_{\text{ext}}(x) dx$

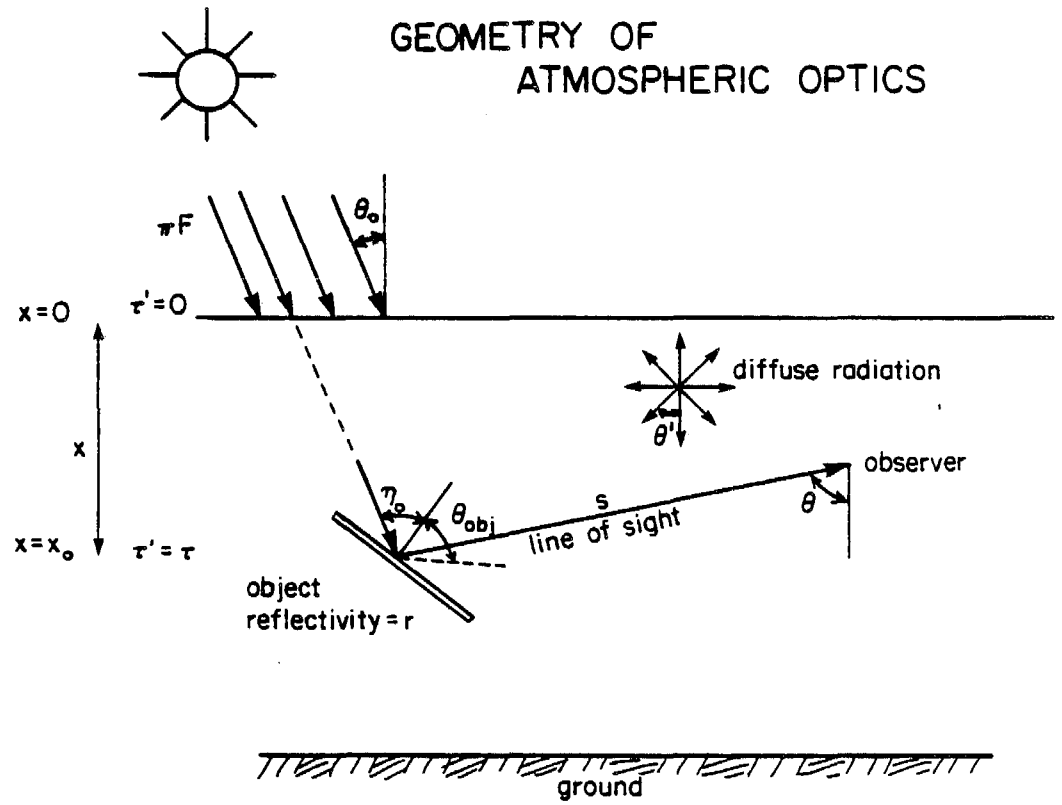
τ_b = optical depth at ground (no
units)

πF = incident solar irradiance,
constant (in units of
watts m^{-2})

ω_0 = single scattering albedo for
the atmosphere (no units)

θ = zenith angle for line of sight
(angle between downward
direction and line of sight);
 $\mu = \cos \theta$

Figure 8



θ_0 = zenith angle for sun;
 $\mu_0 = \cos \theta_0$

θ' = zenith angle for diffuse
 radiation from skylight and
 from ground reflection;
 $\mu' = \cos \theta'$

θ_{obj} = zenith angle for object (angle
 measured with respect to the
 normal to the object);
 $\mu_{obj} = \cos \theta_{obj}$

ϕ = azimuth angle for line of
 sight

ϕ_0 = azimuth angle for sun

ϕ' = azimuth angle for diffuse
 radiation from skylight and
 from ground reflection

ϕ_{obj} = azimuth angle for object

η_0 = angle between sun and normal
 to object

s = path length between object and
 observer (in units of meters)

b_{ext} = extinction coefficient (in
 units of meters⁻¹)

L = the source function (in units of watts m^{-2} steradian $^{-1}$)

M_r = object radiant emittance due to direct solar irradiation (in units of $W m^{-2}$)

p = the phase function for the aerosol as a whole, which describes the probability that light will be scattered in a certain direction (in units of steradian $^{-1}$); $p(\mu_2, \phi_2, \mu_1, \phi_1)$ is the probability that light from direction (θ_1, ϕ_1) is scattered into the direction (θ_2, ϕ_2)

Here equation 1.22 will be reconsidered:

$$I(s) = I(o)e^{-b \text{ext} s} + J(1 - e^{-b \text{ext} s}) \quad (1.22)$$

or in radiance form

$$N(s) = N(o)e^{-b \text{ext} s} + L(1 - e^{-b \text{ext} s}) \quad (4.3)$$

This describes two main contributions to object radiance: (1) light which is reflected from the object and attenuated on its path to the observer and (2) light which is scattered into the observer's line of sight but has not been reflected from the object (the path radiance).

These contributions can be broken down as follows:

- (1) Light from the object:
- (a) direct-direct: Light from the sun that is reflected from the object and transmitted to the observer.
 - (b) diffuse-direct: Diffuse skylight and ground light that is reflected from the object and transmitted to the observer.
- (2) Path radiance:
- (a) single scattering: Light from the sun scattered into the line of sight.
 - (b) multiple scattering:
 - diffuse skylight scattered into the line of sight.
 - ground reflections; light from the ground or other objects scattered into the line of sight.

These contributions can be described mathematically as follows:

(1a) Direct-Direct (from sun to object to observer)

It will be shown that this contribution can be expressed as

$$N(s)_{\substack{\text{direct-} \\ \text{direct}}} = r \cos \eta_0 F \exp(-\tau / \cos \theta_0) \exp(-b_{\text{ext}} s) \quad (4.4)$$

The downwelling radiation from the sun is πF . This radiation is exponentially attenuated along a path which is at an angle θ_0 from the vertical, so that at optical depth τ , the new flux is:

$$\pi F e^{-\tau / \mu_0}$$

where $\mu_0 = \cos \theta_0$. Since the target may be inclined, the flux on the object is

$$\cos \eta_0 \pi F e^{-\tau/\mu_0}$$

The amount reflected from the object gives the radiant emittance from the object, M_r , which is

$$M_r = r \cos \eta_0 \pi F e^{-\tau/\mu_0} \quad (4.5)$$

Another expression for reflected flux can be obtained by integrating the radiance of the object, N_r , over all angles:

$$M_r = \int_0^{2\pi} \int_0^1 N_r \mu_{obj} d\mu_{obj} d\phi_{obj}$$

where $\mu_{obj} = \cos \theta_{obj}$ and ϕ_{obj} is the object azimuth angle.

Since reflectivity is assumed Lambertian,

$$M_r = N_r \int_0^{2\pi} \int_0^1 \mu_{obj} d\mu_{obj} d\phi_{obj} \quad (4.6)$$

$$M_r = N_r \int_0^1 \mu_{obj} d\mu_{obj} \int_0^{2\pi} d\phi_{obj} \quad (4.7)$$

$$M_r = N_r \frac{\mu_{obj}^2}{2} \Big|_0^1 \int_0^{2\pi} d\phi_{obj} \quad (4.8)$$

$$M_r = N_r \left(\frac{1}{2}\right) (2\pi \text{ steradian}) \quad (4.9)$$

$$M_r = N_r \pi \quad (4.10)$$

(Note: The "steradian" unit will be dropped from subsequent equations for ease of notation.)

Equating 4.5 and 4.10 yields the radiance of the object at the location of the object due to direct illumination from the sun.

$$N_r = r \cos \eta_0 F e^{-\tau/\mu_0} \quad (4.11)$$

Over the path from object to observer, this is attenuated by a factor $\exp(-b_{ext} s)$, giving for the direct-direct contribution

$$N(s)_{\substack{\text{direct-} \\ \text{direct}}} = r \cos \eta_o F \exp(-\tau/\cos \theta_o) \exp(-b_{\text{ext}} s) \quad (4.12)$$

(1b) Diffuse-Direct (from skylight to object to observer)

If the scattered radiance field, made up of ambient skylight and ground light, is denoted by N_d , the diffuse-direct contribution can be expressed as

$$N(s)_{\substack{\text{diffuse-} \\ \text{direct}}} = r N_d \exp(-b_{\text{ext}} s) \quad (4.13)$$

since the ambient diffuse radiation falling on the object is reflected from the object and exponentially attenuated over the path length s . N_d can be calculated with a radiative transfer skylight code, as will be discussed. Adding the "direct-direct" and "diffuse-direct" terms:

$$\begin{aligned} & r \cos \eta_o F e^{-\tau/\cos \theta_o} e^{-b_{\text{ext}} s} + r N_d e^{-b_{\text{ext}} s} \\ &= r \left[\cos \eta_o F e^{-\tau/\cos \theta_o} + N_d \right] e^{-b_{\text{ext}} s} \end{aligned} \quad (4.14)$$

The term

$$N(o) = \left[r \{ \cos \eta_o F e^{-\tau/\cos \theta_o} + N_d \} \right] \quad (4.15)$$

is the "inherent radiance," N_o , of an object. Note that, τ depends on b_{ext} . The diffuse flux will change depending on pollutant loading. Therefore N_o is not a constant. In the above derivations, adjacency effects have been ignored. "Adjacency

effects" describe light scattered from other objects into the line of sight or onto the object.

(2) Path Radiance (light which does not hit the object but is scattered into the line of sight)

The path radiance, N_{path} , which arises from light scattered into the line of sight is given in equation 4.3 by:

$$N_{\text{path}} = L (1 - e^{-b_{\text{ext}} s}) \quad (4.16)$$

The source function, L , can be expressed by:

$$L = \omega_0 \frac{F}{4} e^{-\tau/\mu_0} p(\mu, \phi; \mu_0, \phi_0) + \frac{\omega_0}{4\pi} \int_0^{2\pi} \int_{-1}^1 N_d(\tau, \mu', \phi') p(\mu, \phi; \mu', \phi') d\mu' d\phi' \quad (4.17)$$

L is the source function at any point along the optical path and has units of watts m^{-2} steradian $^{-1}$. Two contributions to the source function will be considered:

(2a) Single scattering contribution to L :

The solar flux, πF , is attenuated to an optical depth τ over a slant path: $\pi F e^{-\tau/\mu_0}$. The phase function, $p(\mu, \phi; \mu_0, \phi_0)$, describes the probability that light from the sun is scattered into the observer's line of sight: (to normalize the phase function to unity over all scattering angles, p is divided by 4π):

$$\omega_0 \pi F e^{-\tau/\mu_0} \frac{p(\mu, \phi; \mu_0, \phi_0)}{4\pi} = \omega_0 \frac{F e^{-\tau/\mu_0}}{4} p(\mu, \phi; \mu_0, \phi_0) \quad (4.18)$$

(2b) Multiple scattering contribution:

This arises from scattering of ambient diffuse radiation from all angles into the line of sight. This is expressed by

$$N'_{\text{multiple}} = \left[\frac{\omega_0}{4\pi} \int_0^{2\pi} \int_{-1}^1 N_d(\tau, \mu', \phi') p(\mu, \phi; \mu', \phi') d\mu' d\phi' \right] \quad (4.19)$$

The source function, L , is the sum of these contributions:

$$L = \left[\omega_0 \frac{F}{4} e^{-\tau/\mu_0} p(\mu, \phi; \mu_0, \phi_0) + \frac{\omega_0}{4\pi} \int_0^{2\pi} \int_{-1}^1 N_d(\tau, \mu', \phi') p(\mu, \phi; \mu', \phi') d\mu' d\phi' \right] \quad (4.20)$$

Note that in order to find N_d it is necessary to solve the equation of radiative transfer (1.7), which in radiance form is:

$$\frac{-dN_d}{K\rho ds} = N_d - L \quad (4.21)$$

where L , the source function, in radiance form, is given by equation 4.20. Equation 4.21 is subject to two boundary conditions: one at the top of the atmosphere and one at the ground (Isaacs, 1980). At the very top of the atmosphere ($x=0$), there is only the direct radiation from the sun. Since there are virtually no particles or molecules at this point, the radiance field due to scattering is zero:

$$N_d(0, \mu', \phi') = 0 \quad (\text{bc 1})$$

At the ground, the radiation field consists of reflected sunlight

and skylight. The amount of light directly from the sun, incident on the earth at angle θ_0 , attenuated over the slant path through the atmosphere is:

$$\mu_0 \pi F \exp(-\tau_b/\mu_0)$$

where τ_b is the optical depth at the ground. The diffuse skylight is incident on the earth at angle θ' , from all angles over a hemisphere above the ground:

$$\int_0^{2\pi} \int_0^1 \mu' N_d(\tau_b, \mu', \phi') d\mu' d\phi'$$

The light reaching the ground is reflected isotropically.

$$N_d(\tau_b, \mu, \phi) = \frac{\pi}{\pi} \left[\mu_0 \pi F \exp(-\tau_b/\mu_0) + \int_0^{2\pi} \int_0^1 \mu' N_d(\tau_b, \mu', \phi') d\mu' d\phi' \right] \quad (\text{bc } 2)$$

(boundary condition at ground; see Isaacs, 1980)

There are a variety of different methods that can be used to solve for the radiance field using these boundary conditions and equation 4.21 (Hansen and Travis, 1974). Once N_d is found it can be used in a more complete version of equation 4.3:

$$N(s) = \tau \left[\cos \eta_0 F e^{-\tau/\mu_0} + N_d \right] e^{-b_{\text{ext}} s} + \omega_0 \left[\frac{F}{4} e^{-\tau/\mu_0} p(\mu, \phi; \mu_0, \phi_0) \right. \\ \left. + \frac{1}{4\pi} \int_0^{2\pi} \int_{-1}^1 N_d(\tau, \mu', \phi') p(\mu, \phi; \mu', \phi') d\mu' d\phi' \right] (1 - e^{-b_{\text{ext}} s}) \quad (4.22)$$

If this is written with

$$N(o) = r \left[\cos \eta_o F e^{-\tau/\mu_o} + N_d \right] \quad (4.23)$$

and

$$N^* = \omega \frac{F}{o4} e^{-\tau/\mu_o} p(\mu, \phi; \mu_o, \phi_o) + \frac{\omega_o}{4\pi} \int_0^{2\pi} \int_{-1}^{+1} N_d(\tau, \mu', \phi') p(\mu, \phi; \mu', \phi') d\mu' d\phi' \quad (4.24)$$

the following is obtained:

$$N(s) = N(o) e^{-b_{ext}s} + N^* (1 - e^{-b_{ext}s}) \quad (4.25)$$

For horizon viewing, N^* can be replaced by N_{sky} , the horizon radiance in the direction of view. The equation then becomes

$$N(s) = N(o) e^{-b_{ext}s} + N_{sky} (1 - e^{-b_{ext}s}) \quad (4.1)$$

or if placed in intensity form

$$I(s) = I(o) e^{-b_{ext}s} + I_{sky} (1 - e^{-b_{ext}s}) \quad (1.23)$$

From the above discussion it is clear that $N(o)$, the object inherent radiance, and N_{sky} are not constants but, rather, depend on b_{ext} and thus vary with pollutant loading. This points out several possible problems with Malm's procedure for evaluating the terms in the visibility model tested. The $N(o)$ term obtained from the clean-day photograph by Malm's method could be higher than the actual inherent radiance of an object viewed under polluted conditions. The sky horizon assumption may be invalid, especially for scenes with many objects below the

horizon. Further, determining N_{sky} from the clear day photograph will result in values of N_{sky} that are higher than under polluted conditions, again adding too much brightness to the simulated photo.

Chapter 5

Image Processing—Approach

Image processing is "the manipulation of images by computer" (Castleman, 1979). An image can be visual, like photographs, drawings, or paintings; mathematical, like continuous or discrete functions; or non-visible and physical, like temperature profiles. In order to process an image, a computer must have a numerical representation of the image. The means of converting an image to numerical form is "digitization." The usual method of digitization is to first break up the image into a square grid. Each square of the grid is a picture element, or pixel. A number is then assigned to each pixel. The number could be a measure of the brightness of a photograph, the measurement of a physical property at a point (as for temperature profiles), or the value of a mathematical function at that pixel. During the image processing, these numerical values can be modified in a manner prescribed by the goal of the processing. Once processing is complete, the image can be recreated by reversing the digitization step. For example, a photograph can be recreated or "played back" on a television monitor or on photographic film by displaying brightness values corresponding to the numerical values resulting from the processing. This picture is then referred to as a "playback."

A photograph or slide is a continuous image. A digitized version of a photograph or slide is a discrete description of the

original image. With a small pixel size, the resolution is high and the individual pixels are hard for an observer to discern. This small pixel size means, however, that a large quantity of data must be processed. In this study, each 35 mm slide was grided into an 1800 x 1200 sample pattern, for a total of 2.16×10^6 pixels per picture. In addition, each slide was separated into three color planes—red, green, and blue— which when superimposed result in a full-color slide. To acquire three separate images in the red, green, and blue, the slide is digitized by scanning through optical filters. Three images (6.48×10^6 numerical values) were then needed to describe one full-color image. A series of red, green, and blue Wratten filters (red filter #92, green filter #93, blue filter #94) were used on the digitizer to accomplish the color separation.

When a slide is scanned by a microdensitometer, small areas of the film are sequentially measured for degree of light transmission. The transmission, T (no units), is defined as

$$T = \frac{I_2}{I_1} \quad (5.1)$$

where I_1 is the incident light intensity and I_2 is the transmitted intensity. The optical density (no units) is given by

$$D = - \log T \quad (5.2)$$

The optical density measured is linearly related to numerical density (DN), or gray levels. Numerical density values range from 0 to 255 (0

is black; 128 is gray; 255 is white). Other scales of density level also can be used. At the end of the digitization process, each pixel of each color plane has a numerical density, DN, value.

Production of a synthetic image requires a large number of photographic steps. The original slide must be

1. taken during the field experiments,
2. developed,
3. digitized,
4. processed by computer to render a synthetic photograph,
5. played back onto negative film, and then
6. printed onto color photographic paper

Color photo processing labs can routinely adjust the color balance during processing in order to develop a slide or photograph that "looks good" to the customer. Since the principal objective of this study was to test the radiometric accuracy of the visibility model, it was decided not to permit the repeated color balancing that normally occurs in the photo lab during the processing steps. Deliberate steps were taken to prevent any subjective enhancements of the actual photographs taken. When the slides used in this study were digitized, a standard Kodak #2 steptable gray wedge with 21 steps representing the range of gray levels also was digitized. To correct for any possible distortion of the digital image, the gray wedge was examined, and the correction factors needed to exactly restore the Kodak gray scale were determined. This "gray wedge correction" was then applied to the entire digitized image. This standardized and corrected the digital images for any distortion created while scanning the slides. These gray-wedge-corrected data were used in the production of the

synthetic smog images. After processing, the gray-wedge-corrected data were played back along with a copy of the actual gray wedge which was imbedded in the image. The photo lab was instructed to print the photographs exactly to the gray wedge specification contained on each negative. Statistical tests were applied to gray-wedge-corrected digitized images of synthetic and field photographs. This ensured color control of all images processed and ensured the validity of any comparison between photographs.

Digitizing the clean-day and the actual smoggy-day slides resulted in a description of those slides in terms of numerical density. In order to relate this information to the radiance values required by the model (equation 4.1), the DN values were converted to optical density values, D , using a linear relationship which was determined at the time the original slides were digitized. Then by a polynomial fitting procedure, each of the D vs. E curves, presented in Figure 7, was converted to the form of an equation. These equations were applied to the optical density values to determine the original exposure values for each picture element in each color plane. The exposure values are directly proportional to radiance, N , and are thus used in the visibility model. After applying equation 4.1 to every pixel in the image in order to create a smoggy-day scene, the new exposure values are related back to optical density, then to numerical density. Numerical density is used to obtain a playback of the new synthetic image using a device that writes onto color negative film (the reverse of the digitization step).

In order to create a synthetic smog photograph according to the model tested, a number of separate images are needed.

- (1) The inherent radiance, N_o , for each of the red, green, and blue planes. This is obtained from the clear day slide (April 7, 1983) as prescribed by equation 4.2. The value of b_{ext} used in equation 4.2 is that calculated from the clear day (April 7, 1983) pollutant information.
- (2) A sky radiance, N_{sky} , map for the red, green, and blue. These values also are obtained from the clear day photograph. Sky brightness first was plotted as a function of elevation in degrees above the horizon. The trends were extrapolated for a few degrees below the horizon and then held constant for objects lower than this.
- (3) A distance image. Since equation 4.1 calls for the distance from the observer to the object represented by each pixel, each pixel must have a distance assigned to it. For each photograph, distances from the camera location on the roof of Millikan Library to prominent objects in the field of view were assigned. Using walking surveys, maps and aerial photographs, approximately 400 points were found for the downtown Pasadena scene and 250 points for the San Gabriel Mountain scene. Since an object and its background could be separated by a great distance but have neighboring pixels in a

digitized picture, care was taken to outline individual buildings and geographic features using the distances assigned to the edges of those objects. The remainder of the distance map was created by interpolation between measured points.

Once these images are obtained, equation 4.1 is applied to each pixel in each color plane. The value of b_{ext} is that calculated from the August 25, 1983, pollutant data. (Of course, other values of b_{ext} can be used if other conditions are to be modeled.) The accuracy of the visibility model results are assessed by numerical comparison between this processed image and the digitized version of an actual photograph of the August 25th smog event. The brightness and contrast values are compared for the red, green, and blue planes for the two scenes created. The brightness of each picture is presented in the form of histograms of numerical density, DN, values. The histograms for actual and synthetic photographs are compared. The disappearance of objects from the field of view due to light scattering and absorption is governed by the contrast level between an object and its background, as explained in Chapter 1. Histograms of the absolute value of the contrast between pairs of adjacent picture elements in the clear day, synthetic smoggy day, and the actual smoggy day were prepared and compared.

Following the creation of the synthetic photo of the August 25th smog event, the model was used to illustrate its predictive capability. Synthetic photographs of the August 25th event were

prepared showing the predicted appearance that the downtown Pasadena scene would have on that day if all aerosol carbon was removed from the atmosphere and if all sulfates and associated water were removed.

Chapter 6

Results and Discussion

Two scenes were chosen for digitization and for use in the visibility model evaluation. These scenes were of downtown Pasadena and of the San Gabriel Mountains. Both the clear-day slides and the actual smoggy-day slides were digitized and corrected to the gray wedge. The corrected digitized versions of the clear-day slides are presented in Photographs 1 and 2. The small grain size of the film used to take the original photographs and the small pixel size chosen for the digitization account for the high resolution observed. Features such as radio towers on the mountains are clearly visible. All the photographs presented, unless otherwise noted, are not color enhanced. The gray-wedge correction puts all the photographs and the data on a common basis which is independent of any variation in subsequent film processing. Color-enhanced photographs could be generated in order to present an image more pleasing to the eye, but the original corrected data, keyed to the gray wedge, should be used in making comparisons between the digitized photographs of the actual smog event and the synthetic pictures that result from the visibility model calculations.

Conventional color prints from slides of the actual August 25, 1983, smog episode to be modeled are found in Photographs 3 and 4. These prints have not been digitized, but rather have been produced from slides by a commercial color lab process which includes color

PHOTOGRAPH 1

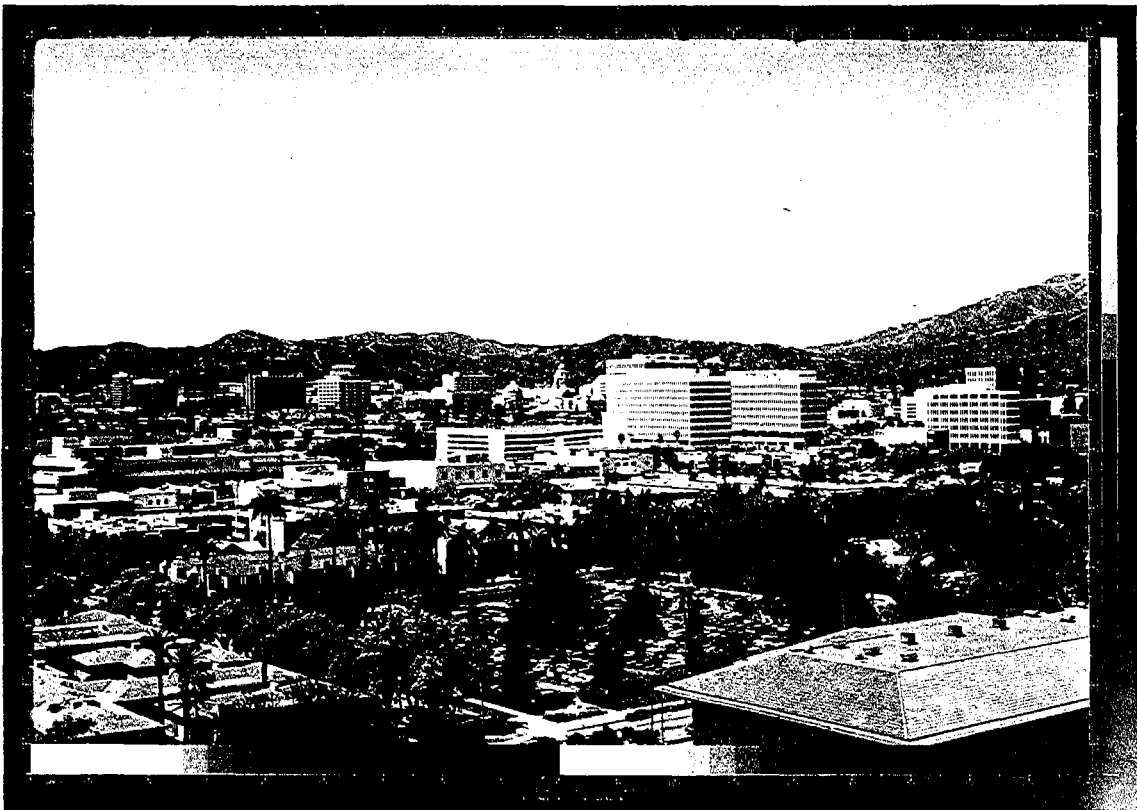
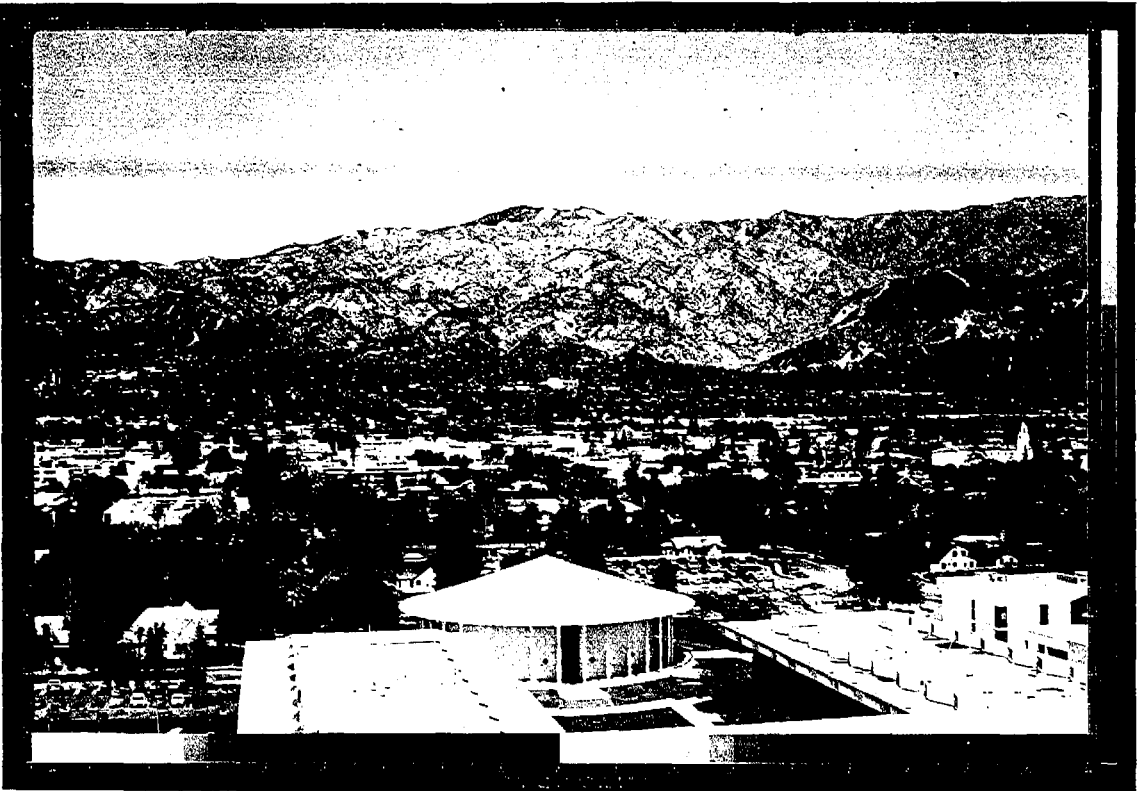
Digitized version of clear day slide (April 7, 1983)
San Gabriel Mountains, gray wedge corrected

P27935

PHOTOGRAPH 2

Digitized version of clear day slide (April 7, 1983)
Downtown Pasadena, gray wedge corrected

P27935



PHOTOGRAPH 3

Conventional print from slide of actual smog event (August 25,1983)
San Gabriel Mountains

P27933

PHOTOGRAPH 4

Conventional print from slide of actual smog event (August 25,1983)
Downtown Pasadena

P27933



balancing to make a product that is preferred by most photographic customers. The slides used to produce these prints were scanned, digitized, and gray-wedge corrected to form a digitized image of the actual smog event. These digitized images are given in Photographs 5 and 6 and are not color enhanced. It is the digitized pictures in Photographs 5 and 6 that will be compared to the synthetic photograph in order to test the accuracy of the visibility model.

The clear-day and smoggy-day digitized photographs form the core of the model application and of the model verification study. Figure 9 gives the overall procedure for the image processing portions of the project. These steps were carried out in order to model the visibility situation on the day captured in the photographs using air pollution information obtained on August 25, 1983. The result is the pair of synthetic photographs presented in Photographs 7 and 8. These synthetic pictures are on the same photographic basis as the clear-day and the actual smoggy-day digitized images. When comparing Photograph 7 to the actual event given in Photograph 5, the general impression is that the visual range (distance to the farthest object visible) and the contrast in both the synthetic images appear to be about correct. When the simulated Pasadena City Hall view (Figure 8) is compared to the digitized actual event (Figure 6), it appears that the contrast and distance to the farthest objects seen are about correct in the center background and right-hand side background of the simulated photo. On the left side of the field of view, a low ridge of mountains can be seen through the haze in the simulated photo that is

PHOTOGRAPH 5

Digitized version of actual smog event (August 25, 1983)
San Gabriel Mountaints, gray wedge corrected

P27932

PHOTOGRAPH 6

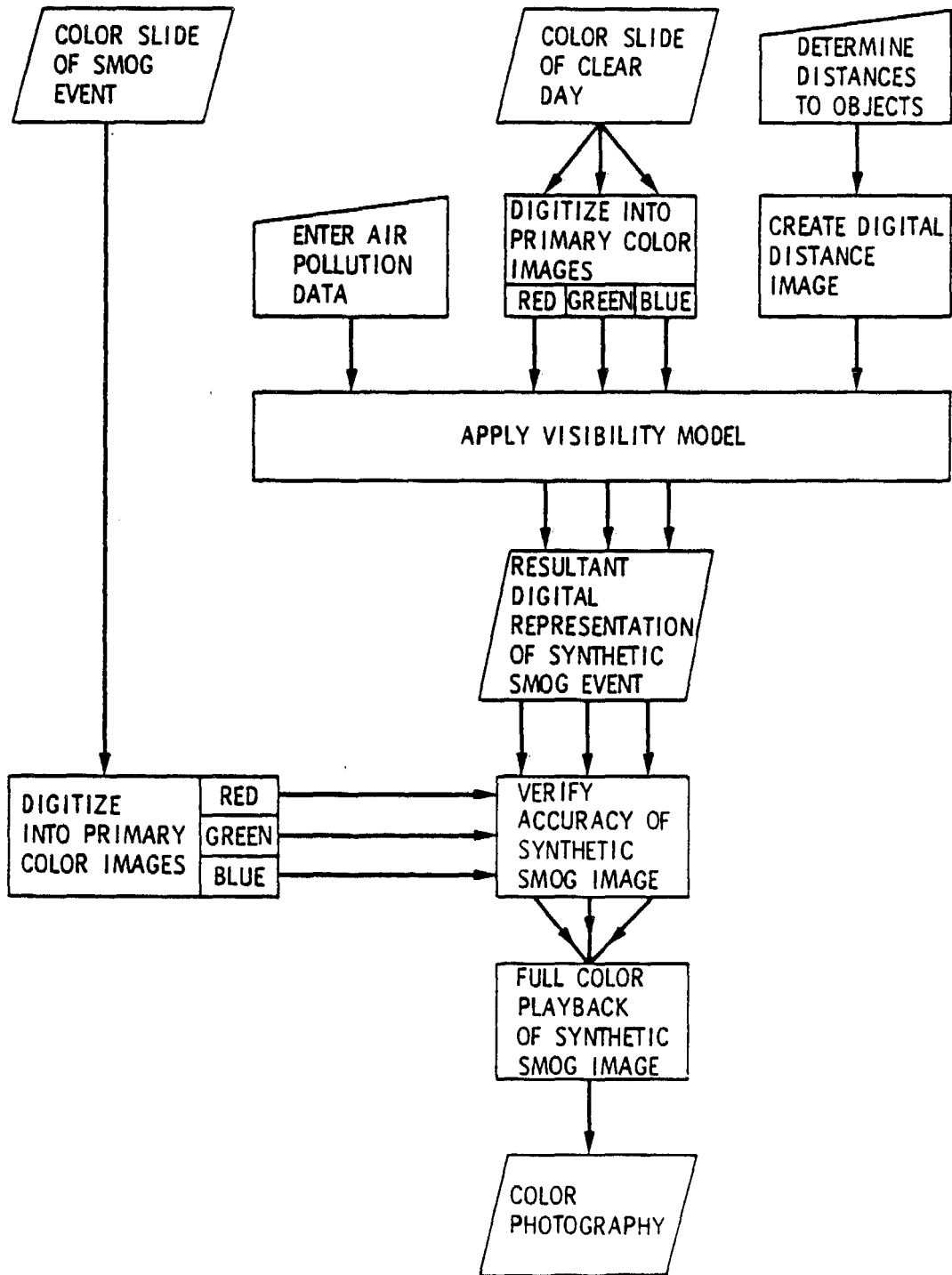
Digitized version of actual smog event (August 25, 1983)
Downtown Pasadena, gray wedge corrected

P27932



Figure 9

IMAGE PROCESSING



PHOTOGRAPH 7

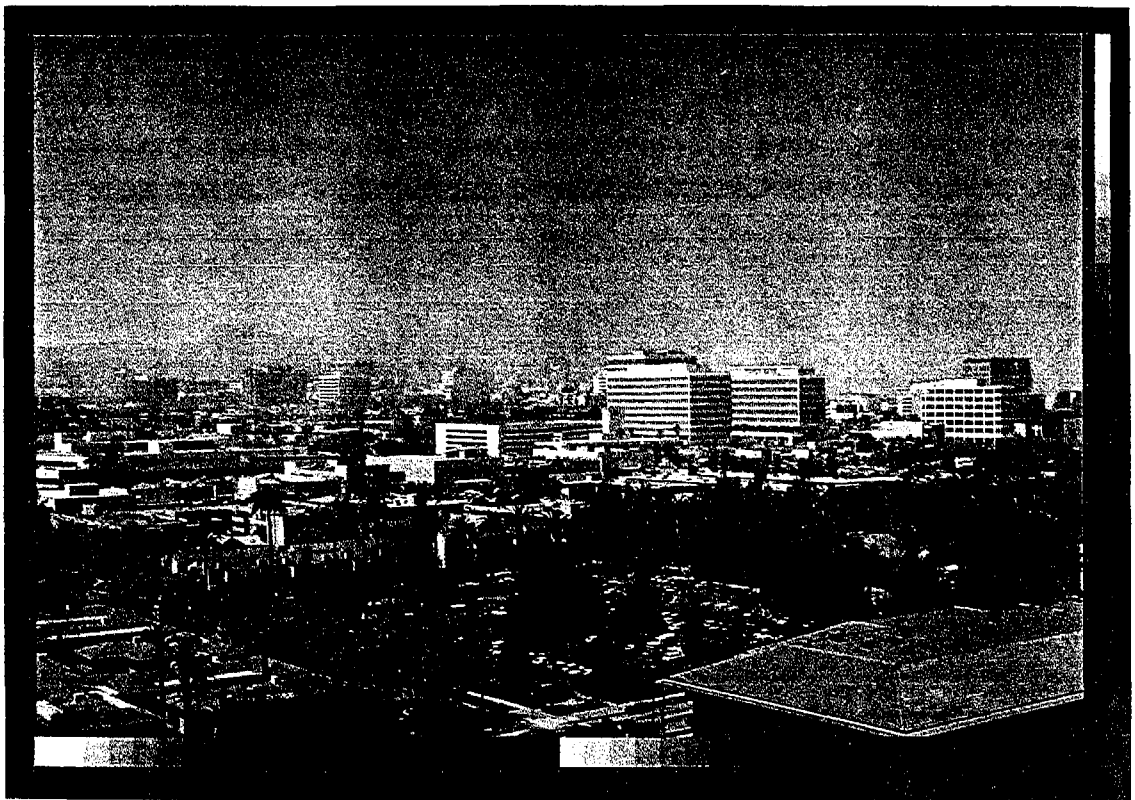
Synthetic image of smog event (August 25, 1983)
San Gabriel Mountains

P27936

PHOTOGRAPH 8

Synthetic image of smog event (August 25, 1983)
Downtown Pasadena

P27936



very difficult to detect in the actual photograph. That ridge happens to fall near the distance to complete visual extinction. Its appearance could be due to horizontal inhomogeneities in the aerosol cloud on the day of interest, or to the fact that the value of $b_{\text{SCAT}_p} + b_{\text{RAYLEIGH}}$ computed from pollutant measurements (and used in the model) falls slightly short of the value of b_{SCAT} measured by the nephelometer (see Table 10). The synthetic smoggy-day photographs (7 and 8) have a blue cast to them when compared to the actual photographs of the smog event. This is due to a fault inherent in the mathematical model used. Too much blue skylight is added to the line of sight. The equation central to the model is, again:

$$N = N_o e^{-b_{\text{ext}}s} + N_{\text{sky}} (1 - e^{-b_{\text{ext}}s}) \quad (4.1)$$

The path radiance term, $N_{\text{sky}} (1 - e^{-b_{\text{ext}}s})$, dominates the object radiance term, $N_o e^{-b_{\text{ext}}s}$, at large distance, s . However, if the value of N_{sky} is sufficiently large, the path radiance term can be significant even for objects located only a relatively short distance from the camera. Analysis of the input data shows that for the red and green color planes, the path radiance makes a significant contribution to the total radiance at large distances and a smaller contribution at short distances. In the blue plane, however, analysis shows that path radiance dominates even for short distances. This is because the sky radiance values, N_{sky} , are based on the appearance of the clear-day sky. Malm's model assumes that the clear-day sky

radiance is also the appropriate sky radiance for use on the smoggy day, while, as shown in Chapter 4, this assumption is not strictly valid. This adds more red, green, and especially blue light to the path radiance than would be the case with a more accurate model. In addition, the model assumes horizon viewing for objects below the horizon and obtains N_{sky} for these points by extrapolating the sky brightness values below the horizon. This extrapolation means that N_{sky} is higher for points below the horizon, and this further increases the value of the path radiance term. Malm's procedure for extrapolation below the horizon should be abandoned in favor of a procedure that more accurately represents the path radiance term in the model.

In order to quantitatively compare the synthetic and actual photographs, numerical density and contrast distributions were plotted for each scene and each color plane. The numerical densities for the clear day and the actual smoggy day were obtained by digitizing the slides of these events. These digital images were gray-wedge corrected. The numerical density for the synthetic photograph was obtained from the visibility model output. Exposure values obtained from corrected numerical density values were used in calculating the contrast between adjacent picture elements in the clear day and the actual smoggy day digital images. For the synthetic smoggy day image, contrast information was obtained from exposure values computed as part of the model output. The contrast is determined by considering adjacent pixel pairs:

$$C(E_1, E_2) = \frac{E_1 - E_2}{E_1} \quad (6.1)$$

where E_1 is the maximum exposure value of the pair.

Numerical density distributions are presented in Figures 10 and 11. It is evident that the synthetic smoggy day which results from the model is fairly close to observations in the red plane but has higher numerical density values than the actual smog event in the blue. To the extent that the model result for the synthetic smoggy day is brighter than the actual smog event at all wavelengths, the combined effect would be to add white light to the picture, making it appear "washed out." The excess brightness shift, however, is most pronounced in the blue plane and is of greater magnitude in the downtown Pasadena view than in the San Gabriel Mountain scene. To the extent that more blue than red or green light is added, the photographs appear both brighter and too blue. The impact of the sky brightness term could be less in the San Gabriel Mountains vista due to a difference in direction and/or to the difference in the amount of sky in the field of view.

The distribution of contrast values between adjacent pixels is shown in Figures 12 and 13. Since this is a comparison of adjacent pixels, a large number of pairs representing pieces of the same object will have low contrast values. Low contrast values also arise for pixel pairs on different objects which are both located at or beyond the distance to visual extinction. Large contrast values are obtained for sharp edges separating light and dark objects. In general, the

Figure 10

Numerical Density Distributions
for San Gabriel Mountains Vista

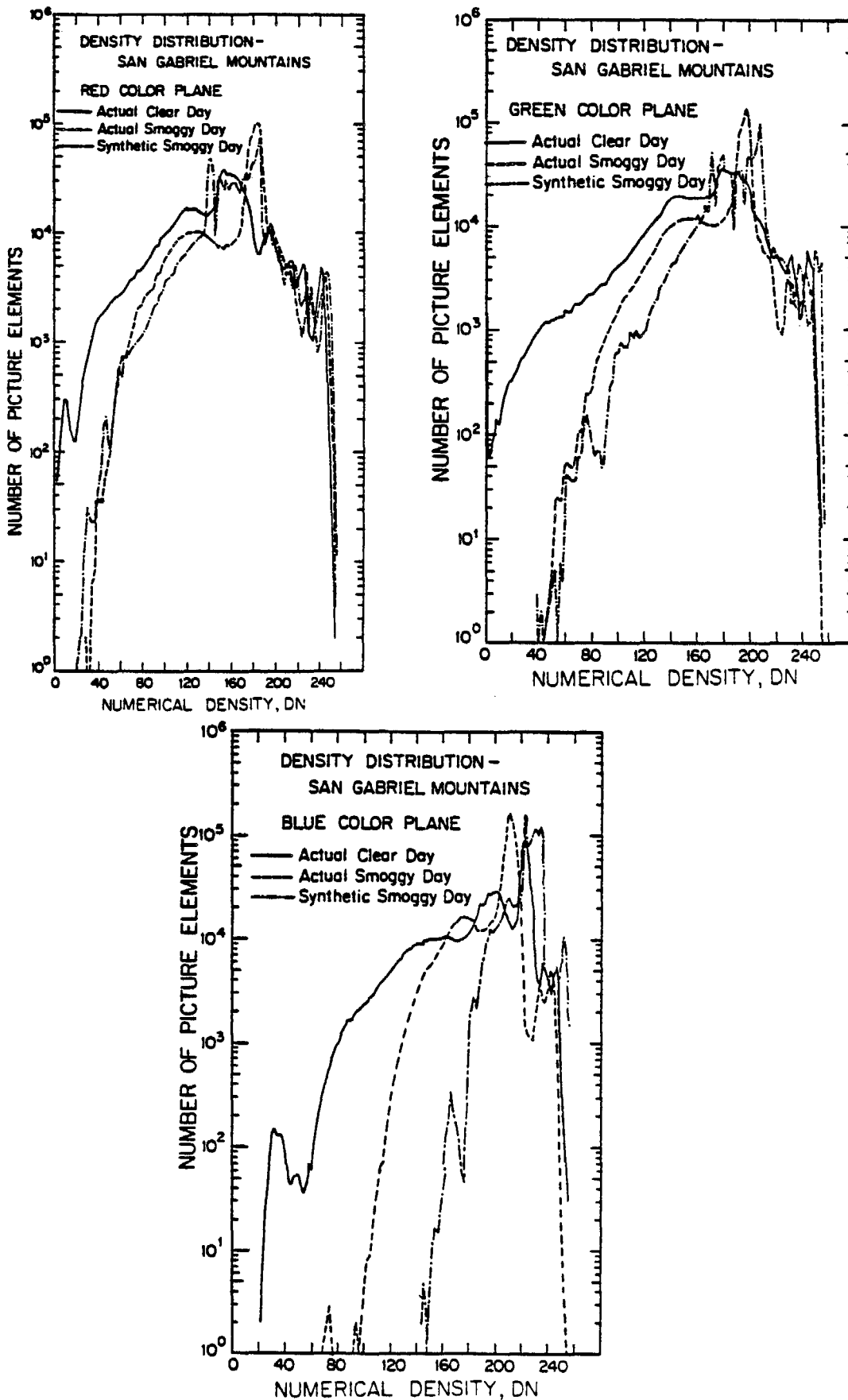
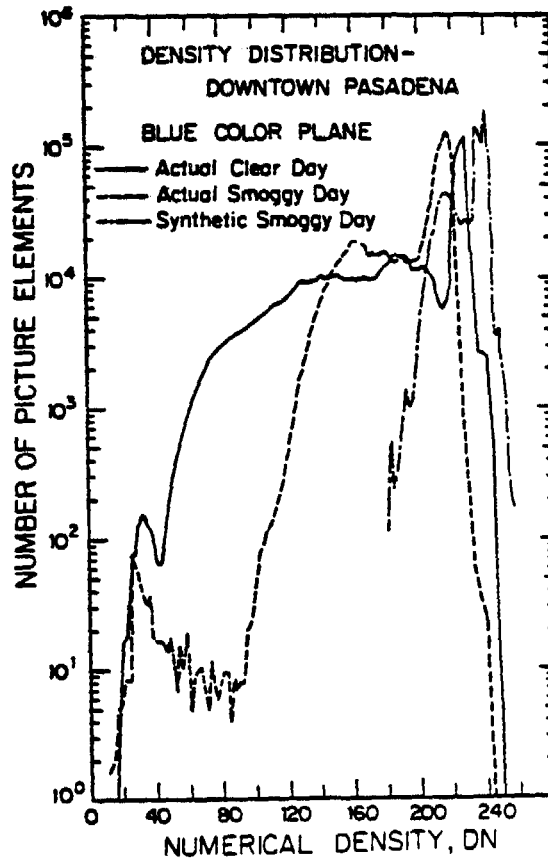
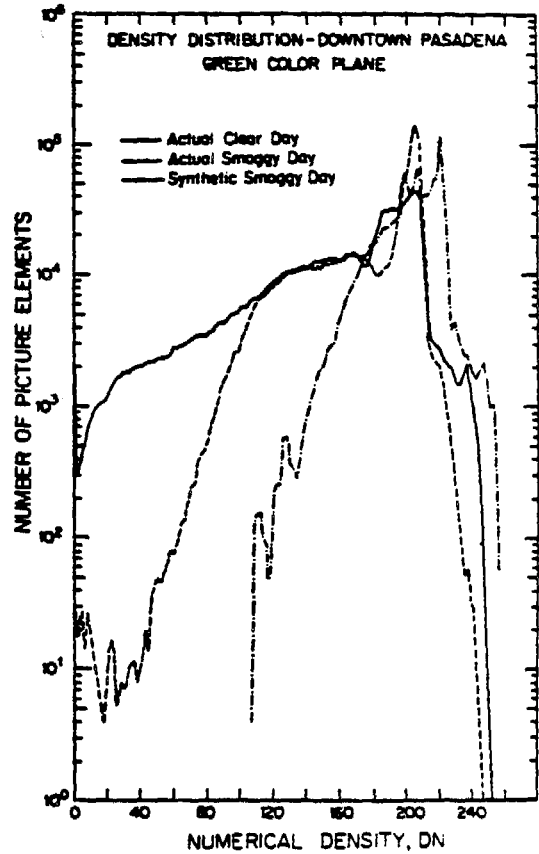
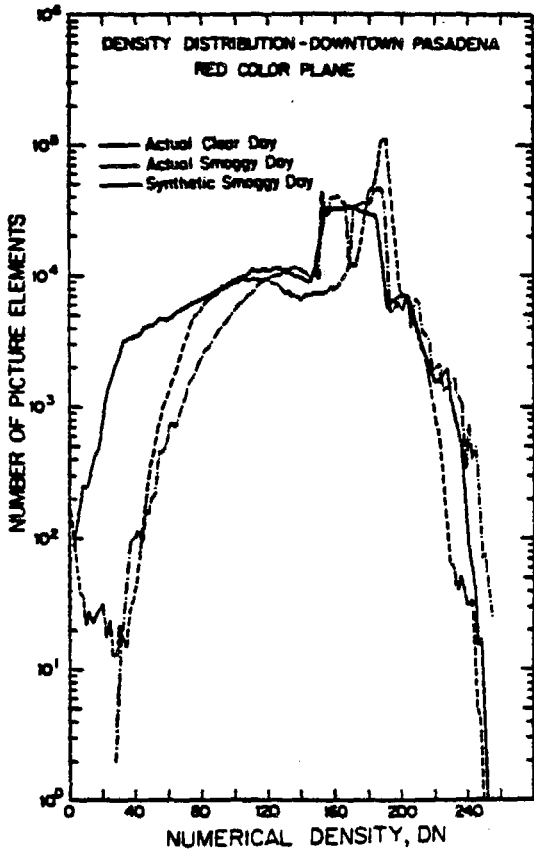


Figure 11

Numerical Density Distributions
for Downtown Pasadena Vista



Contrast Distributions for San Gabriel Mountains Vista

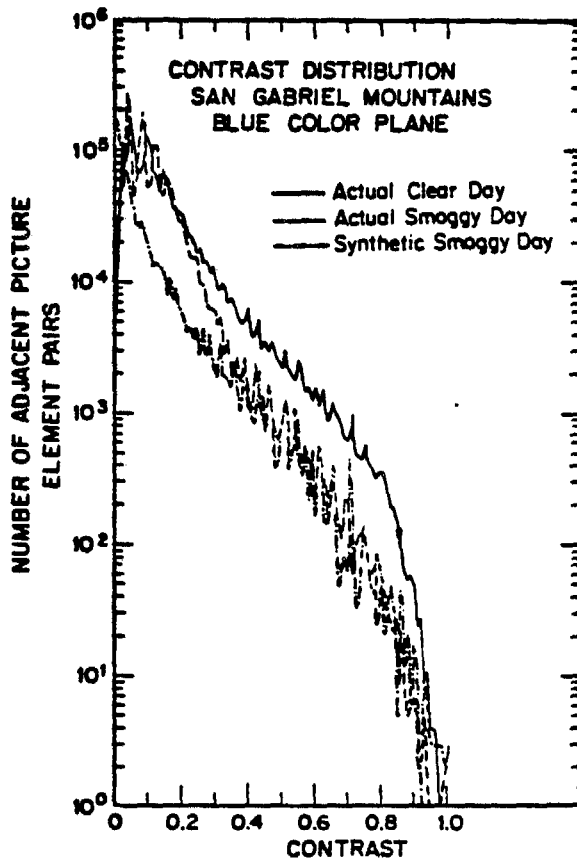
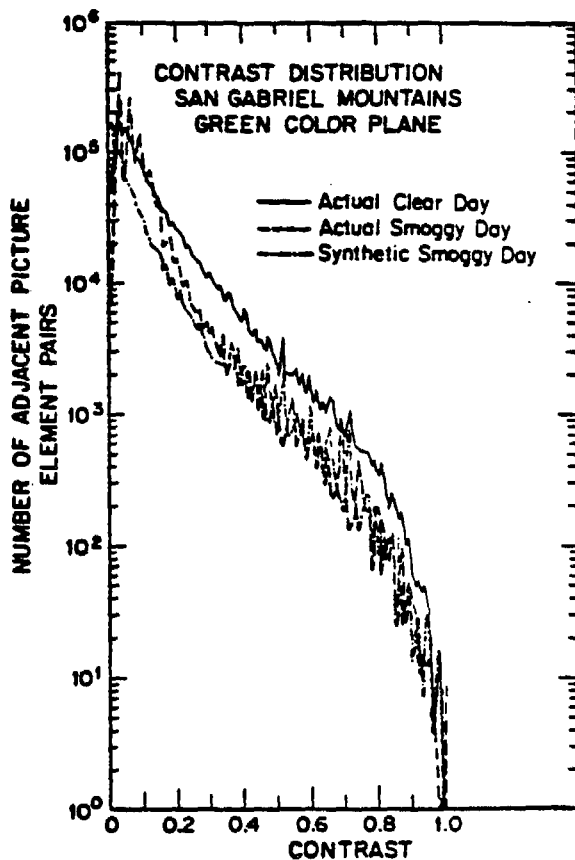
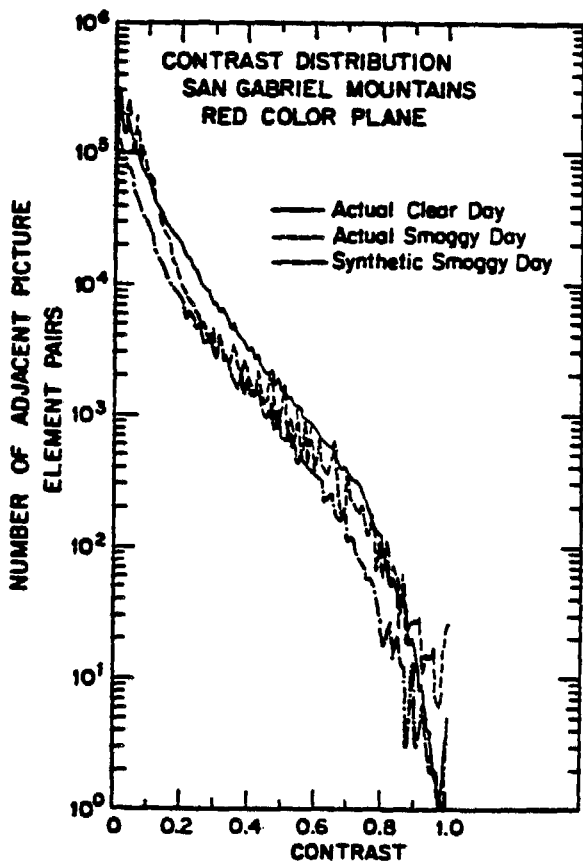
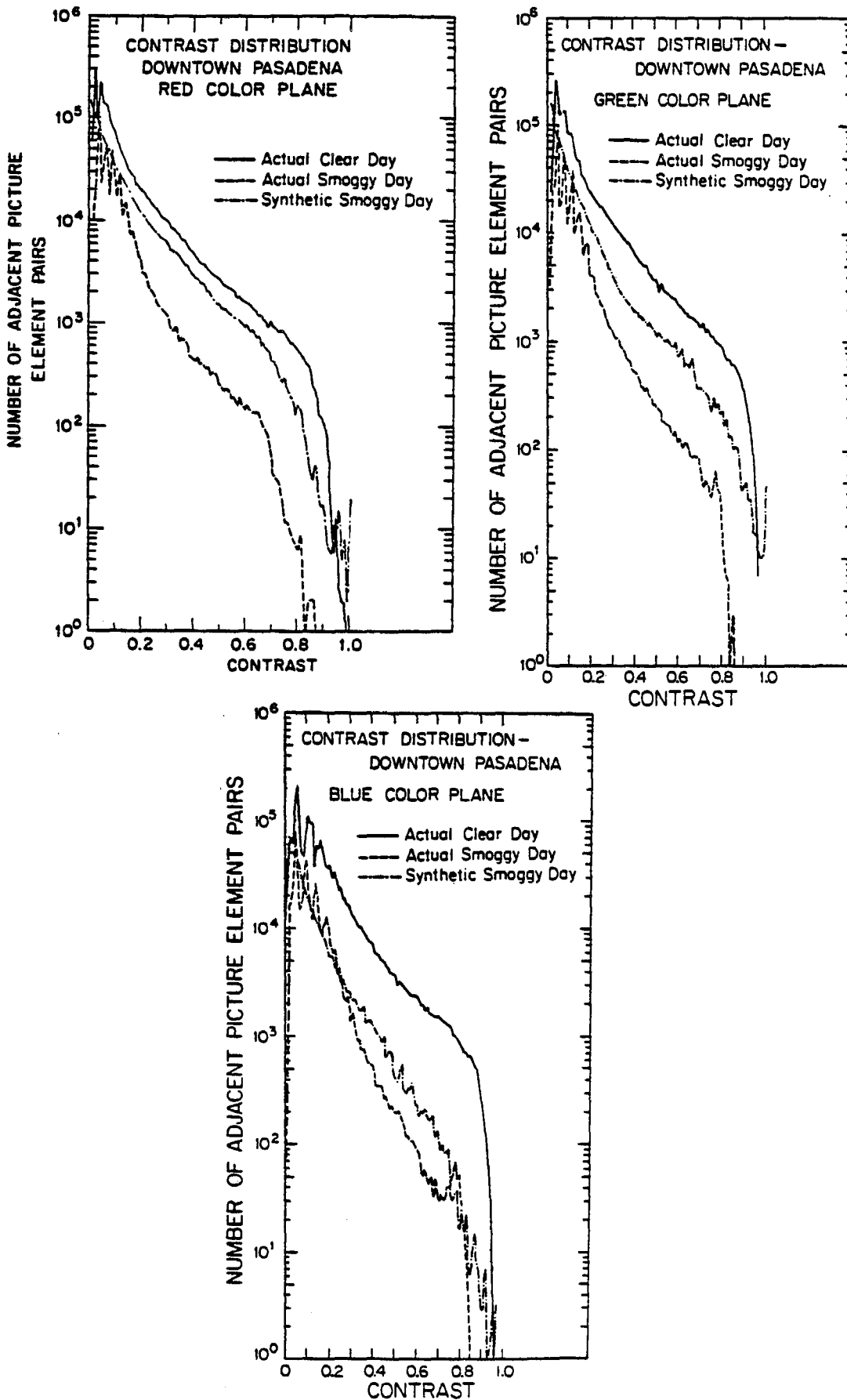


Figure 13

Contrast Distributions for Downtown Pasadena Vista



contrast levels on the synthetic smoggy day image are lower than on the clear day, as expected. For the San Gabriel Mountain scene, the major difference in contrasts in the synthetic and actual smoggy days occurs at the lower contrast range. The contrast difference is higher in the Pasadena scene, where the difference occurs in the larger contrast ranges.

The visibility model can be used as a tool to predict the appearance of a scene given the results of an emission control program. Removing all aerosol sulfates and associated water from the pollutant mixture measured on August 25th, recalculating the aerosol refractive index, and running the model again produces Photograph 10. Removal of all aerosol carbon results in Photograph 9. For this particular day, aerosol carbon removal results in a clearer picture than does the sulfate removal. On the day modeled, visibility reduction was caused to a greater extent by aerosol carbon than by sulfates.

As a result of this investigation, a number of suggestions for improvements in presently available visibility modeling methods can be made. If a "picture postcard" appearance in the final synthetic photograph is desired, then procedures must be developed to permit processing of color-enhanced images without destroying the scientific accuracy of the final product. One possibility for generating synthetic images with color intensities which would match prints produced by color photo laboratories is to correct the digitized clear-day image to match the conventional print of the clear-day

PHOTOGRAPH 9

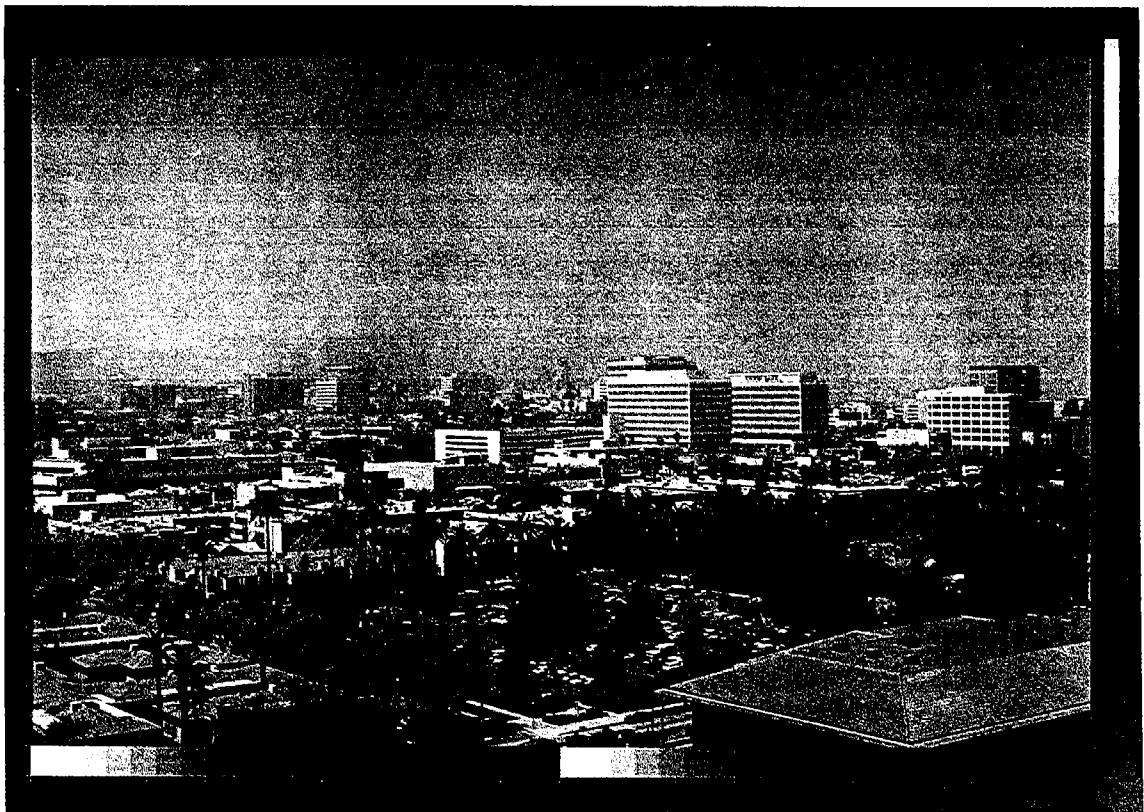
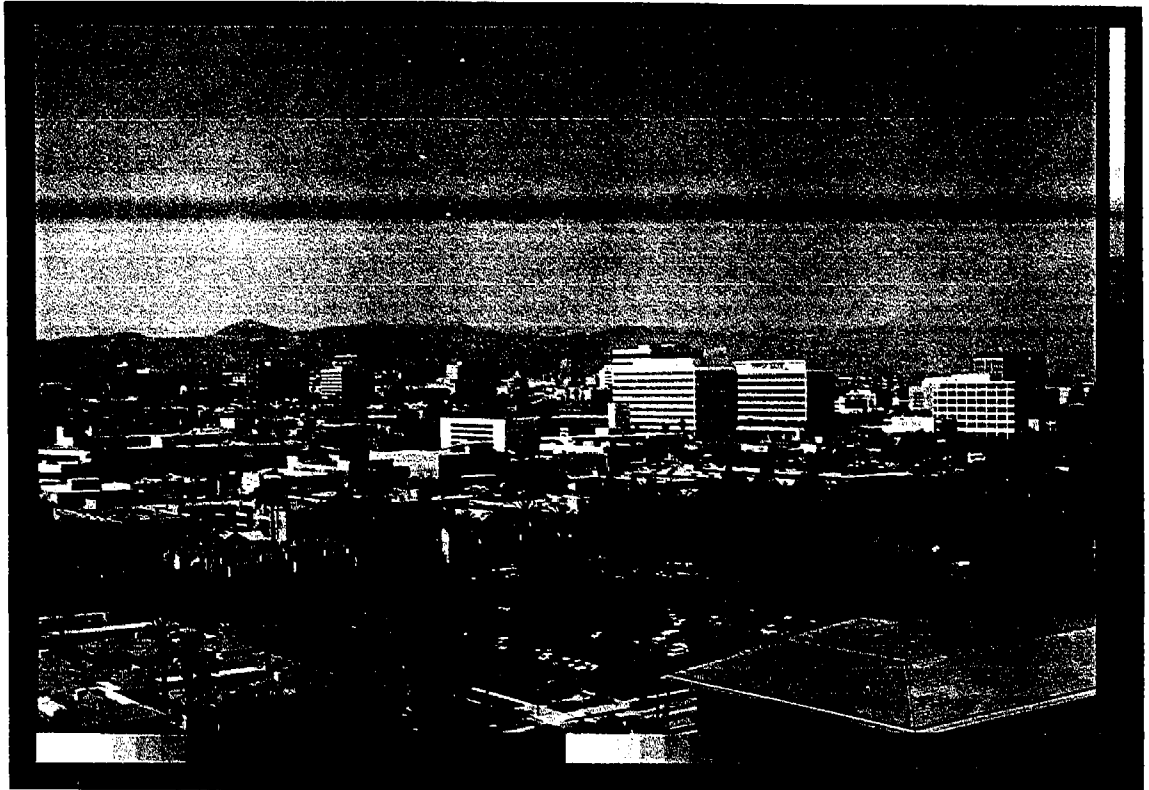
Synthetic image of August 25, 1983, smog event
with removal of all aerosol carbon
Downtown Pasadena

P27934

PHOTOGRAPH 10

Synthetic image of August 25, 1983, smog event
with removal of all sulfates and associated water
Downtown Pasadena

P27934



scene, rather than to correct the digitized image to match the Kodak gray wedge. Photograph 11 shows a conventional print made from an actual slide of the clear day. Photograph 12 shows an attempt to match the digitized base photograph of the same scene to the conventional print. Photograph 12 resulted from instructing the operator of the image processing system to make a perceptual match to Photograph 11. If the data set associated with Photograph 12 was used in the visibility modeling procedure, the resulting synthetic smog photograph may be achieved that is more like the appearance of a conventional print of the actual smog event than was the case for Photographs 7 and 8.

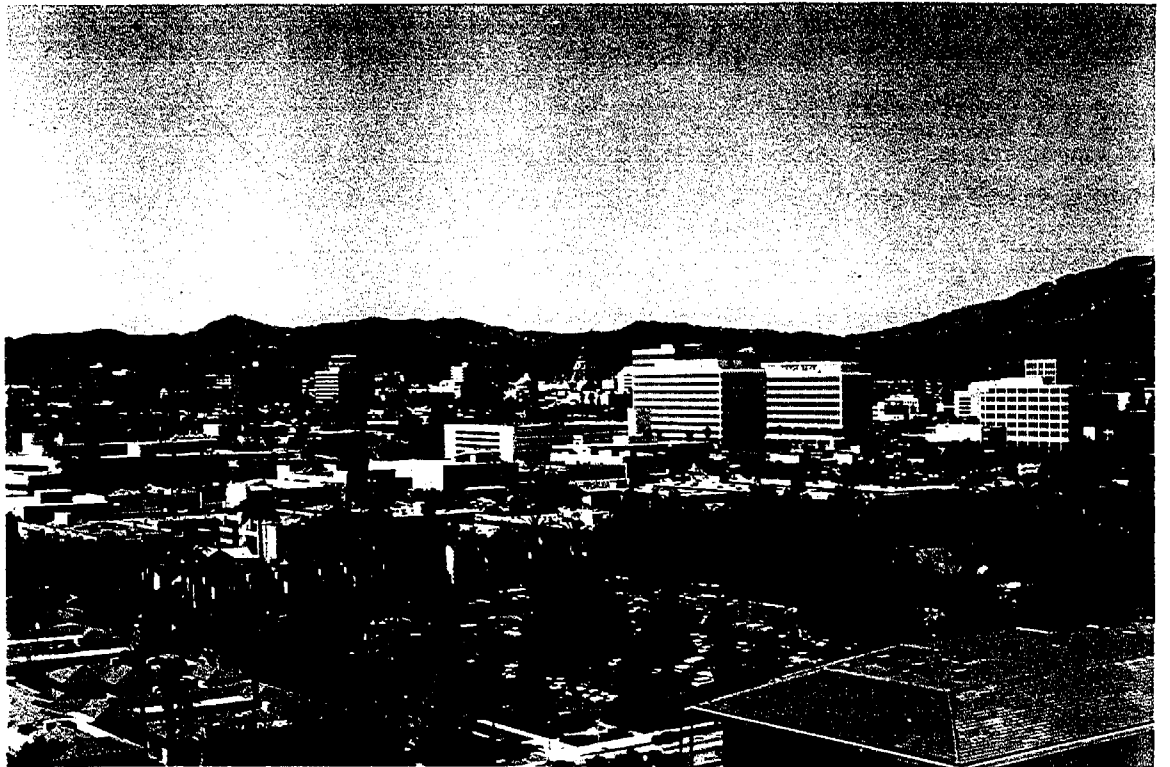
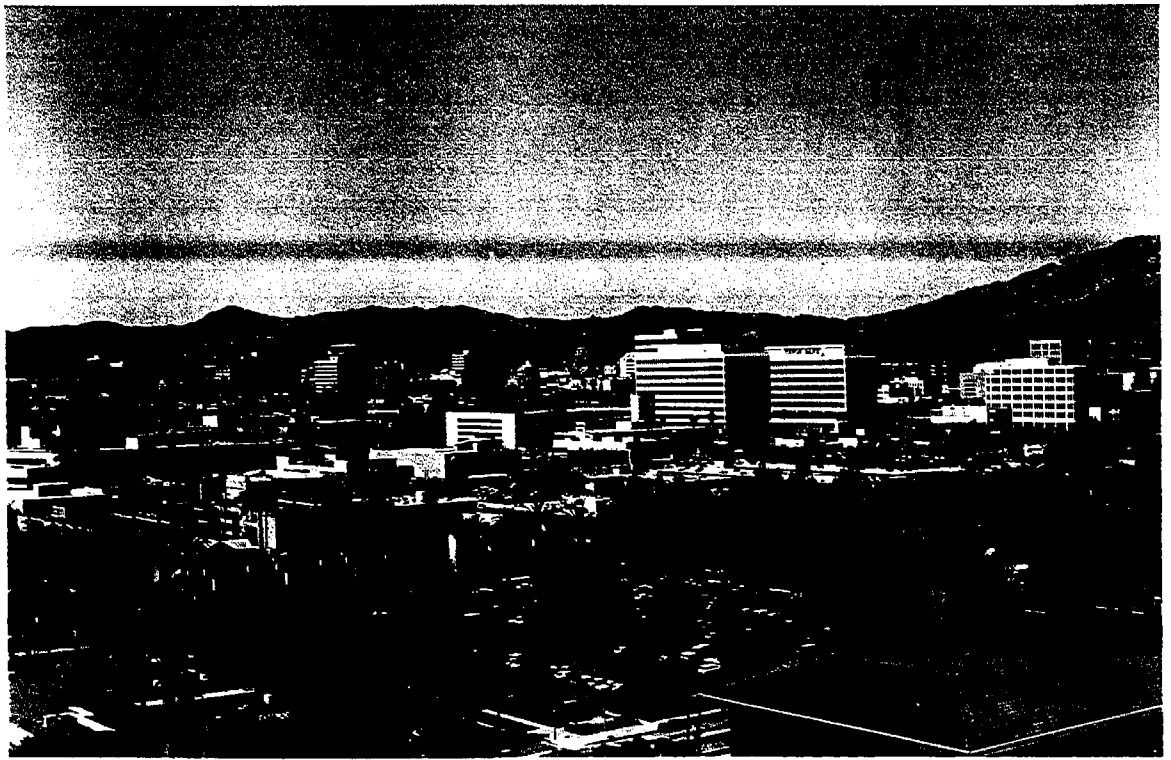
In addition to a color control procedure comparable to commercial photo labs, a better mathematical model needs to be developed. This model should be based on equation 4.22 which more accurately represents the object inherent radiance and the path radiance terms. In that case, multiple scattering, the aerosol phase function, ground reflection, object reflectivity, and atmospheric variations would be considered. Image processing procedures could also be streamlined. The present procedure for handcrafting distance images is very labor intensive. An automated procedure for creating the distance image is feasible and should be developed. The present study compares an entire density or contrast distribution of one photograph to that of another. Pixel-to-pixel comparisons between identical points in the synthetic and actual photographs should be investigated. This type of test will require highly accurate

PHOTOGRAPH 11

Conventional print from slide of actual clear day (April 7, 1983)
Downtown Pasadena

PHOTOGRAPH 12

Digitized version of actual clear day (April 7, 1983)
Downtown Pasadena, color enhanced to create perceptual
match to conventional color print



registration of actual and synthetic images, which could be difficult to achieve. Further advances could be made in the experimental protocol designed to acquire data for use with the model. The ability to measure the chemical composition of the aerosol within narrow size cuts should be improved. Radiance measurements should be taken during the field experiment in order to relate measured photo density to absolute radiance values of specific objects in the scene without reliance on the film manufacturer's density-versus-exposure curves.

Conclusion

Visibility models with synthetic image output show promise as a tool for communicating a great deal of information on how air pollutants can affect the perceived visual quality of a scene. Such models also can be employed to evaluate proposed air pollution abatement programs. But before image-processing-based visibility models can be used with confidence, it is important to be able to quantify the accuracy of their predictions.

This study has developed methods for visibility model verification using image processing techniques. A relatively uncomplicated visibility model proposed by Malm (1983) was chosen for verification testing. Synthetic photographs of defined air pollution situations were compared to actual photographs taken under the conditions modeled. The test procedures indicate that Malm's model approximately reproduces the the contrast degradation present on a smoggy day but overpredicts brightness values, especially in the blue wavelengths, due to an oversimplified treatment of skylight addition. A more accurate visibility model is needed. Specifications for the development of such an advanced visibility model are suggested. The advanced model would incorporate an accurate treatment of multiple scattering, skylight addition, object reflectivity, ground reflection, and aerosol phase function.

A detailed experimental protocol was developed in order to successfully obtain the air pollutant measurements required for the execution of visibility model calculations. Methods for careful image

processing and photographic color control were formulated. These measures ensured that the synthetic photographs produced represent the assumptions inherent in the model tested rather than assumptions built into the input data supplied to the model. This supports the validity of the comparison between real and synthetic images.

References

- Cass, G.R. 1979. On the relationship between sulfate air quality and visibility with examples in Los Angeles. Atmospheric Environment 13:1069-84.
- Castleman, K.R. 1979. Digital image processing. Englewood Cliffs: Prentice Hall.
- Chandrasekhar, S. 1960. Radiative transfer. New York: Dover.
- Countess, R.J., Wolff, G.T., and Cadle, S.H. 1980. The Denver winter aerosol: a comprehensive chemical characterization. Journal of the Air Pollution Control Association 30:1194-1200.
- Dixon, J.K. 1939. The absorption coefficient of nitrogen dioxide in the visible spectrum. Journal of Chemical Physics 8:157-160.
- Groblicki, P.J., Wolff, G.T., and Countess, R.J. 1981. Visibility-reducing species in the Denver "Brown Cloud"—I. Relationships between extinction and chemical composition. Atmospheric Environment 15:2473-2484.
- Hansen, J.E., and Travis, L.D. 1974. Light scattering in planetary atmospheres. Space Science Review 16:527-610.
- Hering, S.V., Flagan, R.C., and Friedlander, S.K. 1978. Design and evaluation of a new low-pressure impactor. 1 Environmental Science and Technology 12:667-673.
- Hering, S.V., Friedlander, S.K., Collins, J.J., and Richards, L.W. 1979. Design and evaluation of a new low-pressure impactor. 2 Environmental Science and Technology 13:184-188.
- Hidy, G.M., et al. 1974. Characterization of aerosols in California (ACHEX). Science Center, Rockwell International. Prepared under California Air Resources Board contract no. 358.
- Hodkinson, J.R. 1966. Calculations of colour and visibility in urban atmospheres polluted by gaseous NO₂. International Journal of Air and Water Pollution 10:137-144.
- Husar, R.B., Holloway, J.M., and Patterson, D.E. 1981. Spatial and temporal pattern of eastern U.S. haziness: a summary. Atmospheric Environment 15:1919-28.
- Isaacs, R.G. 1980. The role of radiative transfer theory in visibility modeling: efficient approximate techniques. Atmospheric Environment 15:1827-1834.

- John, W. and Reischl, G. 1980. A cyclone for size-selective sampling of ambient air. Journal of Air Pollution Control Association 30:872-876.
- Kerker, M. 1969. The scattering of light and other electromagnetic radiation. New York: Academic Press.
- Kodak Color Films 1980. Kodak Publication Number E-77. Rochester, New York: Eastman Kodak Company.
- Lin, C., Baker, M., and Charlson, R.J. 1973. Absorption coefficient of atmospheric aerosol: a method for measurement. Applied Optics 12:1356-63.
- Malm, W., Molenar, J., and Chan, L.L. 1983. Photographic simulation techniques for visualizing the effect of uniform haze on a scenic resource. Journal of the Air Pollution Control Association 33:126-129.
- McCartney, E.J. 1976. Optics of the atmosphere-scattering by molecules and particles. New York: Wiley.
- Middleton, W.E.K. 1952. Vision through the atmosphere. Toronto: University of Toronto Press.
- Nicholls, R.W. 1984. Wavelength-dependent spectral extinction of atmospheric aerosols. Applied Optics 23:1142-1143.
- Ouimette, J.R. 1980. Chemical species contributions to the extinction coefficient. Ph.D. thesis, California Institute of Technology: Pasadena, California.
- Penndorf, R. 1957. Tables of the refractive index for standard air and the Rayleigh scattering coefficient for the spectral region between 0.2 and 20.0 μm and their application to atmospheric optics. Journal of the Optical Society of America 47:176-182.
- Sloan, C.S. 1981. Optical properties of aerosols of mixed composition. General Motors Research Laboratories GMR-4351 ENV #157.
- Sloan, C.S., and Groblicki, P.J. 1981. Denver's visibility history. Atmospheric Environment 15:2631-38.
- Stelson, A.W., and Seinfeld, J.H. 1981. Chemical mass accounting of urban aerosol. Environmental Science and Technology 15:671-79.

Trijonis, J., and Shapland, D. 1979. Existing visibility levels in the United States. U.S. Environmental Protection Agency Report EPA-450/5-79-010.

White, W.H., and Roberts, P.T. 1977. On the nature and origins of visibility-reducing aerosols in the Los Angeles air basin. Atmospheric Environment 11:803-12.

Wickramasinghe, N.C. 1973. Light scattering functions for small particles with applications in astronomy. New York: Wiley.

Williams, M.D., Treiman, E., and Wecksung, M. 1980. Plume blight visibility modeling with a simulated photograph technique. Journal of the Air Pollution Control Association 30:131-134.